

# Investigating ECG Diagnosis with Ambiguous Labels using Partial Label Learning

**SANA RAHMANI**, Department of Electrical and Computer Engineering, Queen's University, Canada

**JAVAD HASHEMI**, School of Computing, Queen's University, Canada

**ALI ETEMAD**, Department of Electrical and Computer Engineering, Queen's University, Canada

Label ambiguity is an inherent problem in real-world electrocardiogram (ECG) diagnosis, arising from overlapping conditions and diagnostic disagreement. However, current ECG models are trained under the assumption of clean and non-ambiguous annotations, which limits both the development and the meaningful evaluation of models under real-world conditions. Although Partial Label Learning (PLL) frameworks are designed to learn from ambiguous labels, their effectiveness in medical time-series domains, ECG in particular, remains largely unexplored. In this work, we present the first systematic study of PLL methods for ECG diagnosis. We adapt nine PLL algorithms to multi-label ECG diagnosis and evaluate them using a diverse set of clinically motivated ambiguity generation strategies, capturing both unstructured (e.g., random) and structured ambiguities (e.g., cardiologist-derived similarities, treatment relationships, and diagnostic taxonomies). Our experiments on the PTB-XL and Chapman datasets demonstrate that PLL methods vary substantially in their robustness to different types and degrees of ambiguity. Through extensive analysis, we identify key limitations of current PLL approaches in clinical settings and outline future directions for developing robust and clinically aligned ambiguity-aware learning frameworks for ECG diagnosis.

## ACM Reference Format:

Sana Rahmani, Javad Hashemi, and Ali Etemad. 2026. Investigating ECG Diagnosis with Ambiguous Labels using Partial Label Learning. 1, 1 (December 2026), 28 pages. <https://doi.org/XXXXXXXX.XXXXXXX>

## 1 Introduction

Electrocardiogram (ECG) signal analysis plays a pivotal role in modern cardiovascular diagnostics, offering a non-invasive and cost-effective means of monitoring the electrical activity of the heart. As cardiovascular diseases (CVDs) remain a leading cause of mortality worldwide, early and accurate detection is essential for effective intervention and treatment [11]. In recent years, advances in signal processing, machine learning, and deep learning have led to the development of automated ECG interpretation systems capable of detecting a wide range of cardiac abnormalities, including arrhythmias. These systems have demonstrated expert-level performance in tasks such as arrhythmia classification [10], contributing to improved diagnostic efficiency and reduced clinical workload. Consequently, automated ECG analysis holds great promise for enhancing the speed, scalability, and reliability of cardiac care in both clinical and remote healthcare environments [22].

---

Authors' Contact Information: **Sana Rahmani**, sana.rahmani@queensu.ca, Department of Electrical and Computer Engineering, Queen's University, Kingston, Ontario, Canada; **Javad Hashemi**, javad.hashemi@queensu.ca, School of Computing, Queen's University, Kingston, Ontario, Canada; **Ali Etemad**, ali.etemad@queensu.ca, Department of Electrical and Computer Engineering, Queen's University, Kingston, Ontario, Canada.

---

Permission to make digital or hard copies of all or part of this work for personal or classroom use is granted without fee provided that copies are not made or distributed for profit or commercial advantage and that copies bear this notice and the full citation on the first page. Copyrights for components of this work owned by others than the author(s) must be honored. Abstracting with credit is permitted. To copy otherwise, or republish, to post on servers or to redistribute to lists, requires prior specific permission and/or a fee. Request permissions from [permissions@acm.org](mailto:permissions@acm.org).

© 2026 Copyright held by the owner/author(s). Publication rights licensed to ACM.

Manuscript submitted to ACM

Manuscript submitted to ACM

1

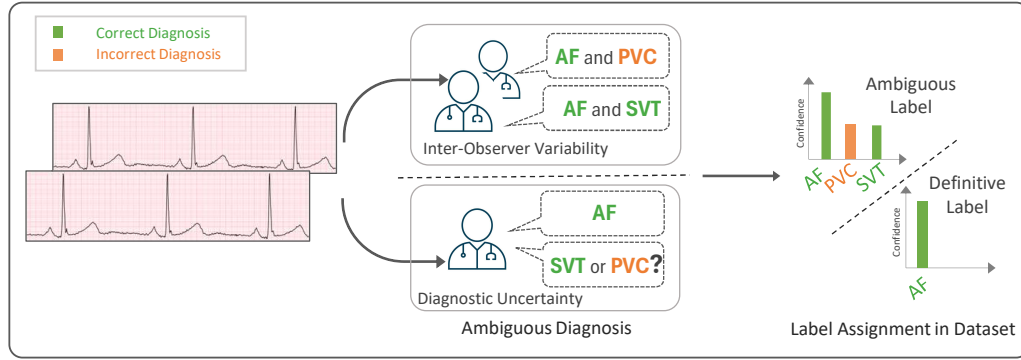


Fig. 1. Ambiguity in ECG diagnosis. Inter-observer variability and diagnostic uncertainty can lead to multiple plausible labels for the same ECG signal. When ambiguity is encountered, the dataset reflects multiple possible diagnoses; when suppressed, a definitive diagnosis is assigned. Selecting definitive labels is the common practice in classic supervised learning approaches.

One of the major challenges in automated ECG interpretation is the possible ambiguity of diagnostic labels. In real-world clinical settings, a single ECG recording may exhibit overlapping features of multiple cardiac conditions, making it difficult for clinicians to assign a definitive diagnosis. Consequently, difficult cases are often reviewed by several clinicians to reach consensus, yet even these procedures are not always successful in completely eliminating all ambiguities [24]. For instance, distinguishing between closely related arrhythmias such as atrial flutter and atrial fibrillation can be difficult, especially in the presence of signal noise or co-occurring patterns [23]. As a result, annotations by medical experts often include multiple possible labels rather than definitive diagnoses [34]. This ambiguity may arise either from inter-observer variability, where different experts assign different diagnoses to the same ECG, or from diagnostic uncertainty within a single expert, who may report several possible conditions (Fig. 1). On the other hand, conventional supervised machine learning models assume precise labels, making them ineffective in scenarios where such ambiguity is common [9, 33].

Unlike conventional supervised learning, Partial Label Learning (PLL) [32] offers an effective framework that can deal with ambiguous labels. PLL methods can learn from samples annotated with a set of *candidate labels* that contains the correct label set. This makes PLL particularly well-suited for biomedical and clinical settings. For example, in single-cell RNA sequencing, different PLL strategies have been used to classify cell types from ambiguous annotations, achieving performance comparable to fully supervised models while significantly reducing the need for manual curation [26]. More recently, PLL has been extended to biosignal analysis tasks such as emotion recognition from electroencephalography (EEG), where ambiguity in self-reported emotional states is common. In these contexts, PLL methods that have been originally developed for image-based classification, have been successfully adapted to model the label ambiguity inherent in human physiological data [46]. Despite success in other biomedical fields, the use of PLL remains largely unexplored in the context of ECG diagnosis.

In this paper, for the first time, we adapt several state-of-the-art PLL methods that have been originally developed for image classification, to the task of cardiac diagnosis using ECG signals. To evaluate these methods under realistic clinical conditions, we construct a comprehensive benchmark based on the PTB-XL [34] and Chapman [49] datasets by introducing controlled ambiguity into the label space. Specifically, we simulate six distinct strategies to reflect real-world diagnostic ambiguity commonly encountered in medical prediction tasks. These strategies are broadly categorized

into three groups: *Random*, *Class-Level* (i.e., Treatment Similarity, Disease Taxonomy Structure, Cardiologist Driven Similarity), and *Instance-Level* (i.e., Model and Cardiologist Driven Similarity). The Class-Level strategies introduce ambiguity based on inter-class similarities (e.g., clinically related conditions), while Instance-Level strategies generate ambiguity by leveraging features of the ECG signal that suggest borderline or uncertain cases. This benchmark enables a systematic and fair comparison of PLL techniques in the context of ECG diagnosis.

Our contributions in this paper are summarized as follows. (1) We introduce PLL to the domain of ECG diagnosis, addressing the challenge of ambiguous labels. To the best of our knowledge, this is the first work to systematically explore PLL for ECG. (2) We adapt and evaluate nine PLL algorithms for the task of ECG classification, providing a comprehensive empirical study on their performance and robustness under varying levels of label ambiguity. (3) We propose and implement six candidate label generation strategies to simulate real-world diagnostic ambiguity in two real-world public datasets, namely PTB-XL and Chapman. (4) To contribute to the area and enable fast reproducibility, we will release our code upon publication.

## 2 Related Work

### 2.1 ECG Signal Analysis

Recent advances in machine learning and deep learning have substantially improved automated ECG analysis, particularly in arrhythmia detection and disease classification. Most progress to date has been driven by supervised learning over large-scale annotated datasets to enable models to learn discriminative representations from ECG signals. Convolutional Neural Networks (CNNs), for example, have demonstrated strong capabilities in feature extraction from ECG waveforms [10]. Deep residual networks [13] have achieved cardiologist-level performance in heartbeat and arrhythmia classification, while Wang et al. [37] proposed a multi-stage model combining convolutional and attention layers to capture complex waveform dependencies. To better model temporal dynamics, hybrid architectures such as CNNs combined with Long Short-Term Memory (LSTM) networks have been explored [44], with Ashahd et al. [2] integrating LSTMs along transformer-based encoders, followed by an uncertainty-aware fusion of their outputs for an effective multi-view processing of ECG signals. More recently, transformer-based architectures such as MCTNet [47] have fused CNNs and self-attention layers to jointly capture local morphology and long-range temporal dependencies, resulting in enhanced classification performance.

Beyond supervised learning, self-supervised and semi-supervised learning approaches have been widely investigated to reduce dependence on large annotated datasets and to address challenges such as label scarcity and distribution shifts. Contrastive self-supervised learning (SSL) methods pre-train models on large collections of unlabeled ECG signals to learn generalizable representations. For example, Liu et al. [18] adopted a BYOL-inspired contrastive framework that improved arrhythmia detection performance compared to fully supervised baselines, while Liu et al. [17] proposed BELL, a multi-branch variant of BYOL tailored for multi-lead ECGs, which leverages intra-lead and inter-lead objectives. Soltanieh et al. [30][29] evaluated several SSL paradigms, including BYOL, SimCLR, and SwAV, showing that pre-trained encoders significantly improve generalization to both in-distribution and out-of-distribution tasks, with SwAV offering the strongest performance. Semi-supervised methods have also been introduced, such as CPSS [28], which combines consistency regularization with pseudo-labeling by assigning positive pseudo-labels to highly confident predictions and negative pseudo-labels to low-confidence categories. By enforcing prediction consistency across weak and strong augmentations, CPSS improves learning from limited labeled data.

Despite these advances in supervised, semi-supervised, and self-supervised ECG analysis, PLL remains largely unexplored in this domain. Unlike semi-supervised learning, which assumes access to both labeled and unlabeled data, PLL assumes that each training instance is associated with a candidate label set containing the true label set but also false positive ones. This paradigm naturally captures real-world annotation scenarios in ECG diagnosis, where diagnostic uncertainty or inter-observer disagreement may result in ambiguous labels. As such, PLL provides a complementary direction to existing weak supervision strategies, with the potential to improve robustness and generalization in automated ECG interpretation. This motivates our adaptation and systematic study of PLL methods for ECG signal analysis.

## 2.2 Partial Label Learning

PLL has emerged as a powerful framework for addressing label ambiguity, where each training instance is associated with a set of candidate labels containing the unknown true label. PLL methods are broadly categorized into two major families: (1) **Average-based methods** treat all candidate labels equally, training the model by averaging supervision signals across all labels in the candidate set. These methods are computationally efficient but often suffer from false positives due to the absence of mechanisms to disambiguate incorrect candidate labels. A representative method is DNPL [27], which employs a custom loss function that assigns higher probability mass to candidate labels without explicitly resolving the ambiguity within the candidate label set. (2) **Identification-based methods**, on the other hand, aim to explicitly infer the ground-truth label from the candidate set by assigning confidence scores to each label and jointly optimizing the model parameters and the label assignments. This class of methods has gained increasing attention for its superior robustness to label ambiguity. For instance, Kim et al. [12] propose filtering out samples with high fluctuations on loss to mitigate ambiguity, although such strategies may inadvertently suppress minority class signals. To overcome class imbalance, the proposed method in [38] introduces an optimization-based disambiguation that accounts for inter-class confidence differences. Similarly, Wang et al. [35] utilize Sinkhorn distance regularization [6] to balance label confidence across classes, thereby improving learning in underrepresented categories.

Several recent methods further enhance label disambiguation by leveraging model parameters. Zhang et al. [45] propose a gradient-based label weighting mechanism, where gradients of model outputs guide candidate label importance. Prototype-based approaches [36] estimate class centroids in embedding space to assign labels via instance-prototype similarity, which are further used to construct supervised contrastive pairs. Similarly, Wu et al. [41] incorporate manifold consistency regularization to enforce label smoothness in the feature space, improving label consistency among similar instances. Beyond architectural strategies, loss function modifications have also proven effective in improving PLL performance. Curriculum learning methods such as [7] introduce a training schedule based on sample difficulty, normalizing the binary cross-entropy (BCE) loss according to candidate label sizes. Other methods explore learning from both candidate and non-candidate labels. Wen et al. [39] apply distinct loss functions to each set: a modified sigmoid loss for candidate labels and a standard sigmoid loss for non-candidate ones. Similarly, the method in [40] employs consistency regularization over augmented inputs to enforce stable predictions under input perturbations, improving generalization under ambiguous supervision. Collectively, PLL methods use architectural, optimization, and loss-based strategies to address label ambiguity. While average-based approaches offer computational simplicity, identification-based methods provide stronger robustness by estimating and correcting label confidences, making them suitable for real-world applications such as medical diagnosis.

### 2.3 PLL in Other Medical Domains

PLL is increasingly used in biomedical domains by enabling models to learn from ambiguous or weakly supervised labels while reducing the dependence on large amounts of expert-annotated data. A prominent application area is single-cell RNA sequencing, where both hierarchical and non-hierarchical PLL strategies have been leveraged to identify cell type, showing accurate classification of transcriptomic profiles is feasible with substantially fewer annotations than required by fully supervised methods [26]. In blood cell classification, Feng et al. [8] proposed a PLL-based strategy that utilizes weakly annotated data in combination with morphological domain knowledge to construct candidate label sets. This method not only improved classification accuracy but also enhanced model interpretability in identifying diverse blood cell attributes. Similarly, in whole slide image (WSI) analysis, PLL has been applied to address the challenge of incomplete labeling. The proposed method in [20] incorporates partial label proportions like subtype ratios among tumor categories, to accurately classify image patches as tumor or non-tumor regions.

Recent work has also explored PLL in the analysis of human biosignals, particularly electroencephalography (EEG) for emotion recognition. Zhang et al. [46] adapted image-based PLL methods to learn from EEG signals, successfully handling label ambiguity during training. To further improve generalization under noisy supervision, Li et al. [14] introduced a generative contrastive loss with feature separability constraints, resulting in more robust models for EEG classification. While these advances illustrate the versatility of PLL across biomedical settings, its application to other physiological signals like ECG, photoplethysmography (PPG), and electromyography (EMG), remains limited. Extending PLL methodologies to these domains presents an important opportunity for developing robust diagnostic systems capable of operating under real-world conditions where label ambiguity is prevalent. In this work, we focus on bridging this gap by exploring the first systematic application of PLL to ECG diagnosis.

## 3 Methods

### 3.1 Preliminaries

Let  $x \in \mathbb{R}^d$  denote an input ECG signal with length  $d$ , and  $\mathcal{Y} = \{1, \dots, C\}$  represent the set of  $C$  possible diagnostic labels. In the PLL framework, each data instance  $x_i$  is associated with a candidate label set  $Y_i \subseteq \mathcal{Y}$ , which contains the unknown ground-truth label set  $\tilde{Y}_i \subseteq Y_i$ . In multi-label settings, the true label set  $\tilde{Y}_i$  may include one or more correct classes, while the remaining classes in  $Y_i$  are the label ambiguities introduced to  $x_i$ . Given a training dataset  $\mathcal{D}_t = \{(x_i, Y_i)\}_{i=1}^n$ , the goal is to learn a multi-label classification model  $\mathbf{f} : \mathbb{R}^d \rightarrow [0, 1]^C$  that estimates a probability distribution over the label set  $\mathcal{Y}$  for each input  $x_i$ . The model should minimize the empirical risk over the ambiguous supervision, where supervision is defined over candidate label sets:

$$\min_{\theta} \left( \frac{1}{n} \sum_{i=1}^n \mathcal{L}(\mathbf{f}(x_i; \theta), Y_i) \right). \quad (1)$$

Here,  $\mathbf{f}(x_i; \theta)$  is the output of the model parameterized by  $\theta$ , and  $\mathcal{L}(\cdot)$  is a PLL-aware loss function that accounts for the ambiguity in  $Y_i$ .

In this work, we adapt and comprehensively analyze nine state-of-the-art PLL algorithms for multi-label ECG classification. These models were selected based on the diverse strategies they employ to address the PLL problem. For example, some approaches focus on contrastive learning to enhance training quality (e.g., Partial Label Learning with Contrastive Label Disambiguation [36]), while others leverage negative supervision to ensure that all available supervision information are utilized (e.g., Consistency Regularization [40] and Leveraged Weighted [39]). Additionally,

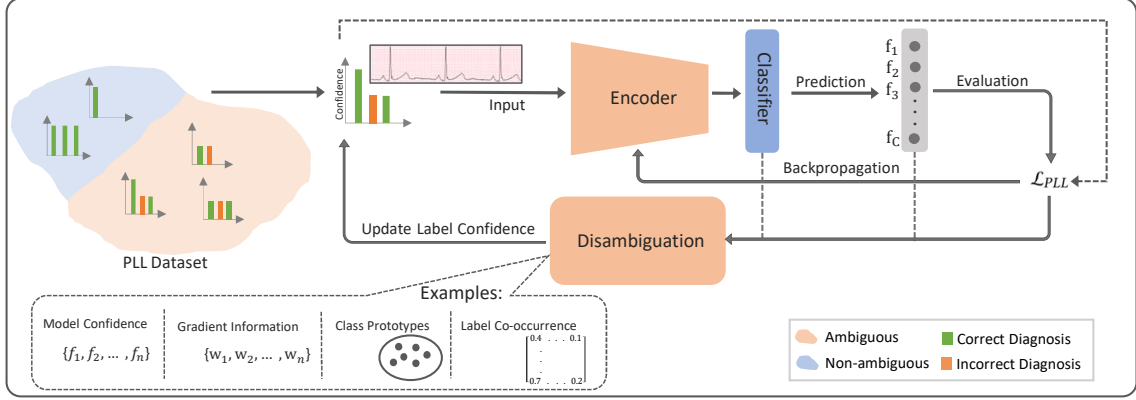


Fig. 2. Overall framework of a PLL-based ECG diagnosis model. The framework integrates an encoder–classifier with a disambiguation module, where candidate label sets are iteratively refined using information such as prediction confidence, and gradient information, while training is guided by an ambiguity-aware loss.

certain methods address multiple challenges inherent in real-world PLL scenarios, such as long-tailed label distributions in the training data (e.g., COrrrection Modification balanCe [48]). To provide clarity and easier comparison across PLL methods, Table 1 summarizes loss function and disambiguation mechanism, while Table 2 compares their components, including integration flexibility, use of semantic information, use of negative supervision, and handling long-tailed distributions. The selected models, described in detail below, were originally developed for image-based tasks and have been adapted here to accommodate the temporal and multi-label nature of ECG signals. Details of our adaptations of PLL baselines are presented within each section below. Each method is evaluated under controlled ambiguity conditions to assess its effectiveness in learning from candidate label supervision.

In Fig. 2, we illustrate the overall framework of a PLL-based ECG diagnosis model. A typical PLL framework consists of two key components: the *Disambiguation* module and the PLL loss function ( $\mathcal{L}_{PLL}$ ). The model is trained on a dataset containing both ambiguous and non-ambiguous samples, which necessitates the use of an ambiguity-aware loss. During training, each input ECG and its candidate label set are fed into the encoder–classifier pipeline to produce predictions, which are optimized via backpropagation. In parallel, the disambiguation module refines the candidate label set by reweighting label confidences based on multiple sources of evidence, such as model prediction scores, gradient information, or label co-occurrence statistics. By iteratively combining disambiguation with supervised optimization, the framework progressively reduces annotation ambiguity and improves classification accuracy.

### 3.2 Deep Naive Partial Label

The Deep Naive Partial Label (DNPL) [27] model performs partial label learning without explicit disambiguation. Instead of attempting to identify the ground-truth label within the candidate label set, DNPL optimizes a naive loss function that encourages the model’s predictions to align with the entire candidate label distribution. The DNPL loss is defined as:

$$\mathcal{L}_{DNPL} = -\frac{1}{n} \sum_{i=1}^n \log (\langle \sigma(\mathbf{f}(x_i; \theta)), Y_i \rangle). \quad (2)$$

Table 1. Comparison of loss functions and disambiguation strategies of different PLL models.

PLL Model	Loss Function	Disambiguation Function
DNPL [27]	$\mathcal{L}_{\text{DNPL}} = -\frac{1}{n} \sum_{i=1}^n \log(\langle \sigma(\mathbf{f}(x_i; \theta)), Y_i \rangle)$	No disambiguation
PRODEN [19]	$\mathcal{L}_{\text{PRODEN}} = \sum_{i=1}^n \min_{y_j \in Y_i} L(f_j(x_i; \theta), y_j)$	$w_{i,j} = \frac{f_j(x_i, \theta)}{\sum_{y_z \in Y_i} f_z(x_i, \theta)}$
CAVL [45]	Supervised cross-entropy loss	$w_{i,j} =  f_j(x_i; \theta) - 1  f_j(x_i; \theta)$
LW [39]	$\mathcal{L}_{\text{LW}} = \sum_{y_j \in Y_i} w_{i,j} L(f_j(x_i)) + \beta \cdot \sum_{y_j \notin Y_i} w_{i,j} L(-f_j(x_i))$	$w_{i,j} = \begin{cases} \frac{e^{f_j(x_i; \theta)}}{\sum_{y_k \in Y_i} e^{f_k(x_i; \theta)}} & y_j \in Y_i \\ \frac{e^{f_j(x_i; \theta)}}{\sum_{y_k \notin Y_i} e^{f_k(x_i; \theta)}} & y_j \notin Y_i \end{cases}$
CR [40]	$\mathcal{L}_{\text{CR}} = -\sum_{y_j \in Y_i} \log(1 - f_j(x_i, \theta)) + \gamma_t \sum_{\tilde{x} \in \tilde{X}_i} KL(p    f(\tilde{x}))$	$p_k = \frac{\left( \prod_{\tilde{x} \in \tilde{X}_i} f_k(\tilde{x}) \right)^{\frac{1}{ \tilde{X}_i }}}{\sum_{y_j \in Y_i} \left( \prod_{\tilde{x} \in \tilde{X}_i} f_j(\tilde{x}) \right)^{\frac{1}{ \tilde{X}_i }}}$ $Y_i \leftarrow \alpha Y_i + (1 - \alpha) \mathbf{w}_i,$
PICO [36]	$\mathcal{L}_{\text{PICO}} = \sum_{i=1}^n (l_{\text{cl}}(x_i, Y_i) + \lambda l_{\text{co}}(x_i))$	$w_{i,j} = \begin{cases} 1 & \text{if } j = \arg \max_{y_j \in Y_i} \mathbf{q}_i^\top \boldsymbol{\mu}_j \\ 0 & \text{otherwise} \end{cases}$
SST [4]	$\mathcal{L}_{\text{SST}} = L_{\text{cls}} + \lambda_1 L_{\text{ist}} + \lambda_2 L_{\text{cst}}$	$\hat{y}_k = \mathbf{1} \left[ \left( \sum_{y_j \in Y_i} p_{k,j}^{\text{ist}} y_j \right) \geq \theta^{\text{ist}} \right]$ $\hat{y}_j^i = \mathbf{1} \left[ \left( \frac{1}{ \mathcal{D}_j } \sum_{x_z \in \mathcal{D}_j} s_{i,z}^j \right) \geq \theta^{\text{cst}} \right]$
HST [3]	$\mathcal{L}_{\text{HST}} = L_{\text{cls}} + \lambda_1 L_{\text{ist}} + \lambda_2 L_{\text{cst}} + \lambda_3 (L_{\text{ist}}^{\text{dtl}} + L_{\text{cst}}^{\text{dtl}})$	(same disambiguation as SST)
COMIC [48]	$\mathcal{L}_{\text{COMIC}} = \lambda_m L_m + \lambda_b L_b + \lambda_c L_c$	$\hat{y}_j = \begin{cases} 1 & \text{if } p_c > \max\{\tau, P_j\}, y_j = 1, \\ 0 & \text{otherwise} \end{cases}$

Here,  $\langle \cdot, \cdot \rangle$  denotes the inner product between the predicted probability vector and the binary candidate label vector, and  $\sigma$  denotes the softmax activation function. This formulation encourages the model to place higher probability on the candidate labels, effectively learning under weak supervision. Since the original DNPL framework was designed for image data, we adapt the architecture to ECG signals by employing a ResNet18 backbone tailored for time-series signals, while retaining the original loss function  $\mathcal{L}_{\text{DNPL}}$  to address the PLL setting. While DNPL does not attempt to resolve ambiguity by estimating true labels, it provides a simple and effective baseline that leverages the structure of candidate label supervision directly in the loss function.

### 3.3 Progressive Identification

The proposed method in PROgressive iDENTification (PRODEN) [19] defines a risk estimator compatible with stochastic optimization for the PLL problem. Accordingly, the PLL loss is defined for classification as the minimum loss among the

Table 2. Overview of different PLL methods. ✓ and × respectively indicate inclusion and exclusion of a component in the method.

Method	Integration Flex.	Neg. Sup.	Semantic Info	Long-tail Handl	Aug. Rep.	Loss Function Design	Disambiguation Strategy	Strengths / Intended Scenarios
DNPL [27]	High	×	×	×	×	Naive PLL loss (inner product with candidate set)	None (naive distribution alignment)	Simple, low complexity
PRODEN [19]	High	×	×	×	×	Refinement-based CE loss	Prediction-based distribution refinement	Lightweight training with disambiguation
CAVL [45]	High	×	×	×	×	Refinement-based CE loss	CAV-based refinement	Low-cost disambiguation via class activation vectors
LW [39]	High	✓	×	×	×	Weighted binary loss on pos./neg. labels	Implicit disambiguation via weighted loss	Leverages all available supervision
CR [40]	Moderate	✓	×	×	✓	Log-likelihood on neg. labels + KL-based consistency loss	Progressive refinement from model predictions	Encourages consistency under augmentations
PICO [36]	Moderate	×	✓	×	✓	Contrastive PLL + log-based classification loss	Contrastive disambiguation	Robust to noisy candidate sets via representation learning
SST [4]	Low	×	✓	×	×	Binary CE + semantic module-specific loss	Per-module refinement with adaptive thresholds	Exploits inter-class and inter-sample dependencies
HST [3]	Low	×	✓	×	×	SST loss + binary CE on thresholds	Threshold-based refinement with automation	Efficient, automated threshold version of SST
COMIC [48]	Moderate	×	✓	✓	×	MFM long-tail loss + balance loss + refinement-based classification	Class-distribution refinement with multi-model balancing	Excels under long-tail distributions and high ambiguity

candidate label set as follows

$$\mathcal{L}_{\text{PRODEN}} = \sum_{i=1}^n \min_{y_j \in Y_i} L(f_j(x_i; \theta), y_j), \quad (3)$$

where  $L$  is the cross entropy loss, and  $f_j$  denotes the model prediction on the  $j^{\text{th}}$  label.

Unlike the DNPL, PRODEN performs disambiguation on the candidate labels parallel to training and tries to converge the model prediction with the disambiguated label set. Accordingly, the *min* operator in Eq. 3 is replaced by dynamic weights  $w_{i,j}$  over the candidate label set which demonstrates the model confidence on each label being the true label. To this end, we initialize the weights uniformly among the candidate set (i.e.,  $w_{i,j} = \frac{1}{|Y_i|}$ ), and further disambiguate this weight in each epoch using model predictions to encourage the possible labels with more weight, as follows

$$w_{i,j} = \frac{f_j(x_i, \theta)}{\sum_{y_z \in Y_i} f_z(x_i, \theta)}. \quad (4)$$

Similar to the DNPL framework, we adapt the PRODEN model for disease classification by employing a ResNet18 backbone designed for time-series. In this adaptation, we retain the original PRODEN loss function  $\mathcal{L}_{\text{PRODEN}}$ , and apply the disambiguation procedure defined in Eq. 4 at each training iteration within our PLL setting.

### 3.4 Class Activation Value Learning

The Class Activation Value Learning (CAVL) [45] method progressively identifies the true label from a candidate label set by estimating the importance of each label based on learned class-specific activation information. CAVL offers an intuitive and gradient-sensitive approach to disambiguate labels without relying on external heuristics. Inspired by Gradient-weighted Class Activation Mapping (Grad-CAM) [25], CAVL computes an importance weight, known as the Class Activation Value (CAV), for each candidate label. This score is derived from the gradient information of the last layer and class-specific output of the model. The CAV for class  $j$  and instance  $x_i$  is computed as:

$$\begin{aligned} w_{i,j} &= \left| \frac{\partial (-\log \sigma_j(f(x_i; \theta)))}{\partial f_j(x_i; \theta)} \right| \sigma_j(f(x_i; \theta)) \\ &= |\sigma_j(f(x_i; \theta)) - 1| \sigma_j(f(x_i; \theta)). \end{aligned} \quad (5)$$

Since the raw model output  $f(x_i; \theta)$  captures richer discriminative information than the class probability  $\sigma(f(x_i; \theta))$ , the softmax activation is removed in practice. This leads to the simplified CAV formulation:

$$w_{i,j} = |f_j(x_i; \theta) - 1| f_j(x_i; \theta). \quad (6)$$

To disambiguate the candidate label set  $Y_i$ , CAVL selects the label with higher CAV importance score among the candidates. As the original CAVL architecture was proposed for image classification, we adapt its disambiguation strategy to disease classification by employing a ResNet18 backbone designed for time-series signals. In this setting, the disambiguated labels  $\hat{y}_i$  are subsequently used to compute the supervised cross-entropy loss during model training.

### 3.5 Leveraged Weighted

Most existing PLL algorithms focus exclusively on candidate labels, often ignoring the complementary information provided by non-candidate classes. To this end, Leveraged Weighted (LW) [39] incorporates both candidate and non-candidate labels into the training process. The core idea is to apply weighted supervision over all classes, where candidate labels are promoted and non-candidate labels are explicitly discouraged. To this end, LW combines candidate and non-candidate labels based on binary loss  $L$  such as sigmoid for a classification loss as follows:

$$\mathcal{L}_{LW} = \sum_{y_j \in Y_i} w_{i,j} L(f_j(x_i)) + \beta \cdot \sum_{y_j \notin Y_i} w_{i,j} L(-f_j(x_i)). \quad (7)$$

Here,  $L(f_j(x_i))$  encourages the model for predictions within the candidate label set and the slightly different component  $L(-f_j(x_i))$  discourages predictions outside the candidate label set. This combination of prediction loss among candidate and non-candidate labels is controlled with a parameter  $\beta$ .

To obtain the weight  $w_{i,j}$ , we normalize the model predictions for both the candidate and non-candidate labels, where:

$$w_{i,j} = \begin{cases} \frac{\exp(f_j(x_i; \theta))}{\sum_{y_k \in Y_i} \exp(f_k(x_i; \theta))}, & y_j \in Y_i \\ \frac{\exp(f_j(x_i; \theta))}{\sum_{y_k \notin Y_i} \exp(f_k(x_i; \theta))}, & y_j \notin Y_i \end{cases} \quad (8)$$

Progressively, this weight is updated to encourage disambiguation of the candidate label set, where a higher weight  $w_{i,j}$  would be given to labels which are more likely to be positive, and ambiguity in labels is further decreased. The disambiguation strategy proposed in LW is applied to obtain the LW loss  $\mathcal{L}_{LW}$ , which is used for training the backbone ResNet18 model on ambiguous ECG signals.

### 3.6 Consistency Regularization

A method similar to LW is adopted in the Consistency Regularization (CR) [40] approach, where non-candidate labels are used in the training objective. CR applies a negative log-likelihood loss over non-candidate labels to exploit the certainty of negative supervision. Additionally, CR introduces a consistency regularization term that enforces the model's predictions to remain stable across different augmentations of the same input, ensuring robust learning from candidate labels. To achieve this, a regularization loss is defined between the model's predictions on a set of augmented inputs  $\tilde{X}_i$  and a conformal label distribution  $p$ . The conformal label distribution is a transformed version of the model's output probabilities, representing the model's confidence across candidate classes. It is initialized with a uniform

distribution and progressively optimized during training based on the model’s predictions as follows:

$$p_k = \frac{\left(\prod_{\tilde{x} \in \tilde{X}_i} f_k(\tilde{x})\right)^{\frac{1}{|\tilde{X}_i|}}}{\sum_{y_j \in Y_i} \left(\prod_{\tilde{x} \in \tilde{X}_i} f_j(\tilde{x})\right)^{\frac{1}{|\tilde{X}_i|}}}. \quad (9)$$

Here,  $f_j(\tilde{x})$  denotes the model’s prediction for class  $j$  on the augmented sample  $\tilde{x}$ . Given an input ECG signal  $x_i$ , we generate a set of augmented views  $\tilde{X}_i = \mathcal{A}(x_i)$  using a data augmentation function  $\mathcal{A}$ . A common practice for augmenting ECG signals [30] is to apply Additive White Gaussian Noise (AWGN), defined as  $\mathcal{A}(x_i) = x_i + \mathcal{N}(\mu, \sigma)$ . This approach enables the generation of both weak and strong augmentations, following the methodology in [46].

The final CR loss at training epoch  $t$  is defined as:

$$\mathcal{L}_{CR} = - \sum_{y_j \notin Y_i} \log(1 - f_j(x_i, \theta)) + \gamma_t \sum_{\tilde{x} \in \tilde{X}_i} KL(p || f(\tilde{x})). \quad (10)$$

The first term penalizes high-confidence predictions on non-candidate labels, preventing predictions on labels not in the candidate label set  $Y_i$ . The second term applies consistency regularization by minimizing the Kullback–Leibler (KL) divergence between the model predictions on augmented inputs and the conformal label distribution  $p$ .

To balance the contribution of the two loss components during training, a dynamic weighting factor  $\gamma_t$  is introduced:

$$\gamma_t = \min\left(\frac{t}{T}\lambda, \lambda\right) \quad (11)$$

Here,  $\gamma_t$  gradually increases over training epochs  $t$  until it reaches a maximum value  $\lambda$  at epoch  $T$ . This annealing strategy emphasizes learning from non-candidate labels in early stages and progressively increases the influence of model prediction consistency, thereby encouraging the model to make confident predictions. We adapt the CR framework to disease classification from ECG signals by employing a ResNet18 backbone tailored for time-series. We then apply the resulting CR loss  $\mathcal{L}_{CR}$  to train the model on ambiguous ECG data.

### 3.7 Partial Label Learning with Contrastive Label Disambiguation

The Partial Label Learning with Contrastive Label Disambiguation (PICO) [36] framework integrates contrastive learning with a prototype-based label disambiguation strategy to enhance representation learning under partial label supervision. Its core idea is to extract class-consistent feature representations and leverage them to assign more accurate soft labels. To this end, PICO defines class prototypes as representative embeddings of each class and updates them progressively.

In supervised contrastive learning, true labels are used to define positive and negative pairs. However, this is infeasible in PLL setting, where the ground-truth label is unknown and the candidate label set may contain false positives. Unsupervised contrastive learning, on the other hand, constructs positive pairs using augmented views of the same input. PICO adopts this strategy by generating two views of an input sample  $x$  using data augmentations  $\mathcal{A}_q$  and  $\mathcal{A}_k$ , producing query and key embeddings:  $\mathbf{q} = g(\mathcal{A}_q(x))$  and  $\mathbf{k} = g'(\mathcal{A}_k(x))$ , where  $g$  and  $g'$  are encoder networks.

Key embeddings are stored in a queue to form an embedding pool:  $A = B_q \cup B_k \cup \text{queue}$ , and the positive set is defined as  $p(x) = \{x' \in A(x) \mid f(\mathcal{A}_q(x')) = f(\mathcal{A}_q(x))\}$ , where  $A(x) = A \setminus \{\mathbf{q}\}$ . The contrastive loss is then defined by contrasting the query embedding against all embeddings in the embedding pool:

$$l_{co}(x) = -\frac{1}{|p(x)|} \sum_{x'' \in p(x)} \log \frac{\exp(\mathbf{q}^\top x'' / \tau)}{\sum_{x' \in A(x)} \exp(\mathbf{q}^\top x' / \tau)}, \quad (12)$$

where  $\tau$  is a temperature scaling factor.

In addition to contrastive learning, PICO includes a classification loss to guide predictions toward the candidate labels:

$$l_{\text{cl}}(x, Y) = \sum_{y_j \in Y} -y_j \log(f_j(x; \theta)). \quad (13)$$

The total loss of PICO combines both components:

$$\mathcal{L}_{\text{PICO}} = \sum_{i=1}^n (l_{\text{cl}}(x_i, Y_i) + \lambda l_{\text{co}}(x_i)), \quad (14)$$

where  $\lambda$  balances the contribution of the classification loss.

To support label disambiguation, class prototypes  $\boldsymbol{\mu}_j$  are updated as the mean of embeddings assigned to class  $j$  by the classifier  $\boldsymbol{\mu}_j \leftarrow \text{avg} \{ \mathbf{q}_i \mid j = \arg \max f(\mathcal{A}_q(x_i)) \}$ .

Using these prototypes, each candidate label set  $Y_i$  is refined using a moving average update:

$$Y_i \leftarrow \alpha Y_i + (1 - \alpha) \mathbf{w}_i, \quad (15)$$

$$\mathbf{w}_{i,j} = \begin{cases} 1 & \text{if } j = \arg \max_{y_j \in Y_i} \mathbf{q}_i^\top \boldsymbol{\mu}_j \\ 0 & \text{otherwise,} \end{cases} \quad (16)$$

where  $\alpha \in [0, 1]$  controls the smoothing rate. This update gradually aligns the candidate labels with the most semantically similar prototypes, facilitating more confident disambiguation. We adapt the PiCO framework to disease classification from ECG by employing a ResNet18 backbone. During training, we apply the disambiguation process defined in Eq. 16 together with the PiCO loss  $\mathcal{L}_{\text{PICO}}$  to train the model.

### 3.8 Structured Semantic Transfer

Structured Semantic Transfer (SST) [4] is a PLL framework that enhances label disambiguation by exploiting structured semantic relationships between classes. Unlike conventional PLL methods that rely solely on candidate label sets, SST explicitly models inter-class correlations and transfers semantic structures to guide learning under ambiguity, thereby improving prediction, consistency, and robustness.

The SST framework begins by encoding an input ECG signal  $x_i$  into a feature representation  $\phi_i$  using a backbone neural network. In our adaptation, we employ a ResNet18 backbone to extract ECG-specific representations, which are then passed to subsequent modules for further processing. These features are further refined through a semantic decoupling [5] module that generates class-specific, semantic-aware representations  $\tilde{\phi}_{i,j}$  for each class  $j$ . In the original SST design for image classification, class semantics are derived from pre-trained word embeddings. However, to ensure a fair comparison of partial label learning capabilities across all evaluated methods, we restrict the use of external resources such as pre-trained language models or ontology-based embeddings. Instead, we replace the original class semantic vectors with prototype embeddings computed as the centroid of ECG signals belonging to each class. This design choice isolates the effect of the semantic decoupling architecture itself, enabling us to assess its contribution under identical information constraints for all models. Although centroid-based embeddings may lack the external semantic richness of word embeddings, they provide a dataset-derived proxy for class semantics.

In this module, the feature representation  $\phi_i$  is fused with the semantic embedding  $e_j$  via low-rank bilinear pooling as follows:

$$\tilde{\phi}_{i,j} = \mathbf{P}^T \left( \tanh \left( \left( \mathbf{U}^T \phi_i \right) \odot \left( \mathbf{V}^T e_j \right) \right) \right) + \mathbf{b}, \quad (17)$$

where  $\tanh$  is the hyperbolic tangent function,  $\odot$  denotes element-wise multiplication, and  $\mathbf{P}$ ,  $\mathbf{U}$ ,  $\mathbf{V}$ , and  $\mathbf{b}$  are learnable parameters. The resulting semantic-aware representations are then passed through a sigmoid-activated classifier to produce the output probabilities  $\mathbf{p}_i$ .

Given that certain classes are semantically correlated, the SST framework leverages inter-class dependencies to enrich class-specific representations. In ECG analysis, for instance, some conditions frequently co-occur, and capturing these relationships can improve label disambiguation. To model such correlations, we construct an adjacency matrix  $A \in [0, 1]^{C \times C}$  that encodes class co-occurrence patterns. Specifically, in our adaptation,  $A$  is derived directly from the partial labels in the ECG training dataset, ensuring that the graph captures clinically meaningful dependencies as closely as possible without relying on ground-truth labels. Each entry  $A_{j,k}$  is defined as the probability of observing class  $k$  given class  $j$ , computed as the number of times classes  $j$  and  $k$  co-occur divided by the total number of occurrences of class  $j$ . This matrix defines a weighted graph over the class space, where edges represent co-occurrence strength between classes. A Gated Graph Neural Network (GGNN) [15] is then applied to propagate information across this graph, enabling class-specific representations to be contextually refined based on their related classes.

**Intra-image Semantic Transfer (IST).** To refine label estimates within each sample, the IST module constructs a class co-occurrence matrix based on semantic-aware features. Although originally proposed for images, this module is employed for ECG signals without any architectural modifications. For a pair of classes  $j$  and  $k$ , their co-occurrence probability is calculated as:

$$p_{j,k}^{ist} = f^{ist}([\tilde{\phi}_{i,j}, \tilde{\phi}_{i,k}]), \quad (18)$$

where  $f^{ist}$  is a neural network composed of fully connected layers, and  $[\cdot]$  denotes feature concatenation. This yields a matrix  $P_i^{ist} \in \mathbb{R}^{C \times C}$  capturing the co-occurrence strength of class pairs. The refined label estimate for class  $k$  is then given by:

$$\tilde{y}_k = \mathbf{1} \left[ \left( \sum_{y_j \in Y_i} p_{k,j}^{ist} y_j \right) \geq \theta^{ist} \right], \quad (19)$$

where  $\theta^{ist}$  is a predefined threshold, and  $\mathbf{1}[\cdot]$  is the indicator function. The IST module is trained using a loss function that encourages high co-occurrence scores for observed label pairs and penalizes unlikely prediction combinations:

$$L^{ist} = \sum_{(y_j, y_k) \in B_i} (1 - p_{j,k}^{ist})^{\gamma_1} \log(p_{j,k}^{ist}) + \sum_{(y_j, y_k) \notin B_i} (p_{j,k}^{ist} - m)^{\gamma_2} \log(1 - p_{j,k}^{ist}), \quad (20)$$

where  $B_i$  denotes the set of label pairs in the candidate set  $Y_i$ , and  $\gamma_1$ ,  $\gamma_2$ , and  $m$  are hyperparameters.

**Cross-image Semantic Transfer (CST).** Complementing IST, the CST module captures inter-sample relationships, assuming that inputs with similar semantic content likely share labels. Similar to the IST module, although CST was originally proposed for images, it is employed for ECG signals without any architectural modifications. For a given class  $j$ , the similarity between semantic-aware features of two inputs  $x_i$  and  $x_z$  is computed via cosine similarity:

$$s_{i,z}^j = \cos(\tilde{\phi}_{i,j}, \tilde{\phi}_{z,j}). \quad (21)$$

The refined label for class  $j$  in sample  $x_i$  is then estimated as:

$$\tilde{y}_j^i = \mathbf{1} \left[ \left( \frac{1}{|\mathcal{D}_j|} \sum_{x_z \in \mathcal{D}_j} s_{i,z}^j \right) \geq \theta^{cst} \right], \quad (22)$$

where  $\mathcal{D}_j$  is the set of samples containing class  $j$ , and  $\theta^{cst}$  is a predefined similarity threshold. The CST loss encourages high similarity prediction between related ECG samples:

$$L^{cst} = \sum_{z=1}^N \sum_{y_j \in Y_i} (1 - s_{i,z}^j). \quad (23)$$

**Classification Loss.** SST employs a partial binary cross-entropy loss to handle ambiguous labels:

$$\ell(\mathbf{p}_i, Y_i) = \frac{1}{|Y_i|} \left( \sum_{y_j \in Y_i} \log(p_j^i) + \sum_{y_j \notin Y_i} \log(1 - p_j^i) \right). \quad (24)$$

This loss is computed not only on the original candidate labels  $Y_i$ , but also on pseudo-labels obtained from the IST and CST modules, denoted as  $\hat{Y}_i$  and  $\tilde{Y}_i$ , respectively. The final classification loss becomes:

$$L_{cls} = \sum_{i=1}^N \left( \ell(\mathbf{p}_i, Y_i) + \ell(\mathbf{p}_i, \hat{Y}_i) + \ell(\mathbf{p}_i, \tilde{Y}_i) \right). \quad (25)$$

The total loss for the SST framework integrates all components:

$$\mathcal{L}_{SST} = L_{cls} + \lambda_1 L_{ist} + \lambda_2 L_{cst}, \quad (26)$$

where  $\lambda_1$  and  $\lambda_2$  control the contributions of the IST and CST modules, respectively. Accordingly, we apply the SST loss  $\mathcal{L}_{SST}$  to train our ECG classification model under PLL setup.

### 3.9 Heterogeneous Semantic Transfer

Heterogeneous Semantic Transfer (HST) [3] builds upon the SST framework by introducing key enhancements aimed at improving efficiency and adaptability in PLL. While the backbone network and the IST module remain similar to those in SST, the CST module is significantly improved. Instead of computing pairwise similarities between samples, HST introduces class prototypes to efficiently capture inter-sample semantics.

For each class  $j$ , semantic-aware representations of samples containing class  $j$  are clustered using k-means to form  $k$  prototypes  $\{\tilde{p}_{1,j}, \dots, \tilde{p}_{k,j}\}$ . Given an input  $x_i$ , the similarity to class  $j$  is computed by averaging cosine similarities between  $\tilde{\phi}_{i,j}$  and the class prototypes:

$$s_i^{j,k} = \cos(\tilde{\phi}_{i,j}, \tilde{p}_{k,j}), \quad \hat{y}_i^j = \mathbf{1} \left[ \left( \frac{1}{K} \sum_{k=1}^K s_i^{j,k} \right) \geq \theta^{cst} \right]. \quad (27)$$

This strategy reduces computational cost while preserving semantic alignment. The CST loss remains similar to SST:

$$L^{cst} = \sum_{z=1}^N \sum_{y_j \in Y_i} (1 - s_{i,z}^j). \quad (28)$$

**Differential Threshold Learning (DTL).** To eliminate the need for manual threshold tuning in the IST and CST modules of SST model, HST introduces the DTL module. Traditional threshold-based pseudo-labeling is sensitive to the values of  $\hat{\theta}^{ist}$  and  $\theta^{cst}$ , which are often dataset-specific. DTL addresses this by reformulating thresholding as a differentiable process, enabling the thresholds to be learned end-to-end via gradient descent.

For IST and CST, DTL defines the threshold difference scores as:

$$d_i^{j,IST} = \left( \sum_{y_j \in Y_i} p_{k,j}^{ist} y_j \right) - \theta^{ist}, \quad d_i^{j,CST} = \left( \frac{1}{K} \sum_{k=1}^K s_i^{j,k} \right) - \theta^{cst}. \quad (29)$$

These values are then used to supervise the threshold learning using partial binary cross-entropy:

$$L_{ist}^{dtl} = \sum_{i=1}^N \ell \left( Y_i, \mathbf{d}_i^{IST} \right), \quad L_{cst}^{dtl} = \sum_{i=1}^N \ell \left( Y_i, \mathbf{d}_i^{CST} \right), \quad (30)$$

where  $\ell$  denotes the partial binary cross-entropy loss. By leveraging the candidate labels as supervision, DTL dynamically learns suitable thresholds that balance recall and precision, improving robustness to ambiguous labels.

**Classification Loss.** Similar to SST, HST computes classification loss over the original candidate labels as well as the pseudo-labels generated by IST and CST. The total training objective for the HST model is:

$$\mathcal{L}_{HST} = L_{cls} + \lambda_1 L_{ist} + \lambda_2 L_{cst} + \lambda_3 \left( L_{ist}^{dtl} + L_{cst}^{dtl} \right), \quad (31)$$

where  $\lambda_1$ ,  $\lambda_2$ , and  $\lambda_3$  are hyperparameters that control the contribution of each component. Similar to SST, we apply the HST loss  $\mathcal{L}_{HST}$  to train our ECG classification model, incorporating the enhanced CST design and adaptive threshold learning to improve efficiency and performance under partial label supervision.

### 3.10 COrrECTION ModificatIon balanCe

PLL methods often face significant challenges when dealing with datasets that exhibit a *long-tailed* label distribution and multiple forms of imbalance. In such scenarios, two types of imbalance commonly occur: (1) a *head-tail* (major-minor) class imbalance, where a few head classes have abundant samples while many tail classes are underrepresented; and (2) a *positive-negative* imbalance, where each instance contains only a few positive labels but many negative labels. These imbalances, combined with label ambiguity, can cause models to overfit to frequent head classes, underfit rare tail classes, and be dominated by the overwhelming number of negative labels, leading to poor generalization. COrrECTION, ModificatIon, balanCe (COMIC) [48] addresses this challenging setting by unifying three complementary components: (1) a class-frequency-aware loss function, named Multi-Focal Modifier (MFM), that incorporates both inter-instance head-tail balancing and intra-instance positive-negative balancing; (2) a parallel head-tail balanced learning architecture with cross-model knowledge distillation; and (3) a label correction mechanism that iteratively refines candidate label sets. The integration of these modules enables COMIC to simultaneously disambiguate candidate labels, mitigate both forms of imbalance, and enhance robustness under ambiguous supervision.

**MFM loss.** To address imbalance in label frequency, COMIC adopts a modified Focal Loss [16] tailored for long-tailed data. The MFM loss reduces emphasis on head classes while amplifying the gradient contribution from tail classes. This is achieved through dynamic scaling factors that combine intra-sample and inter-class imbalance metrics, ensuring that underrepresented classes receive proportionally higher attention. The intra-sample factor controls the positive-negative weighting within a sample, while the inter-class *head-tail factor* increases with class imbalance degree, further emphasizing rare classes. Given predicted probability  $p$  for the  $j^{\text{th}}$  class, the MFM loss is defined separately for positive and negative labels as:

$$L_m^+ = \sum_{j=1}^C (1 - p_j)^{y_j^+} \log(p_j), \quad L_m^- = \sum_{j=1}^C p_j^{y_j^-} \log(1 - p_j), \quad (32)$$

where  $\gamma_j^+$  and  $\gamma_j^-$  control sensitivity for positive and negative samples, respectively:

$$\gamma_j^+ = \gamma^{pn^+} + w^+ \cdot \gamma_j^{ht}, \quad \gamma_j^- = \gamma^{pn^-} + w^- \cdot \gamma_j^{ht}. \quad (33)$$

Here,  $\gamma^{pn^+}$  and  $\gamma^{pn^-}$  are intra-sample positive–negative scaling factors, with  $\gamma^{pn^-} \geq \gamma^{pn^+}$  to upweight positive samples;  $w^+$  and  $w^-$  are coefficients that adjust inter-class weighting; and  $\gamma_j^{ht} \geq 1$  is the head–tail imbalance factor reflecting the imbalance degree of class  $j$  with higher values for minor classes. This loss formulation amplifies the gradient contribution of positive samples from tail classes while reducing overemphasis on head classes or negative samples.

**Head–Tail Balancer.** Even with reweighted loss functions, extreme imbalance can cause head classes to overfit and tail classes to underfit. To counter this, COMIC trains three parallel models with different learning rate decays: a head-class expert  $\mathcal{M}_h$ , a tail-class expert  $\mathcal{M}_t$ , and a balanced model  $\mathcal{M}_b$ . While an ECG signal is passed through these models, the balanced model aggregates features from the two head and tail models via an additive attention mechanism, producing a shared representation for classification, as follows:

$$\phi_b = \text{Attn}(\hat{\phi}_b, [\phi_h, \phi_t]) + \hat{\phi}_b, \quad (34)$$

where  $\phi_h$ ,  $\phi_t$ , and  $\hat{\phi}_b$  are the feature embeddings from  $\mathcal{M}_h$ ,  $\mathcal{M}_t$ , and  $\mathcal{M}_b$ , respectively.

A multi-head classifier normalizes class logits by dividing the  $k^{\text{th}}$  weight vector  $w_k$  into  $q$  groups:

$$\mathbf{z}_x = \frac{\rho}{q} \sum_{k=1}^q \frac{w_k^\top \phi_x}{(\|w_k\| + \eta) \|\phi_x\|}, \quad x \in \{h, t, b\}, \quad (35)$$

where  $\rho$  is a scaling factor and  $\eta$  is a class-agnostic baseline energy.

To further enforce balance, the model’s optimization bias is estimated from the moving average of accumulated gradients:

$$\mathbf{e}_t = \mu \cdot \mathbf{e}_{t-1} + \text{sum}(g_t), \quad (36)$$

where  $\text{sum}(g_t)$  aggregates the gradients at iteration  $t$ . This vector  $\mathbf{e}_t$  is added and subtracted respectively from the logits of  $\mathcal{M}_h$  and  $\mathcal{M}_t$  to simulate balanced training on major and minor classes:

$$\hat{\mathbf{z}}_x = \mathbf{z}_x \pm \frac{\rho}{q} \sum_{k=1}^q \frac{\text{sim}(\mathbf{z}_x, \mathbf{e}_t) \cdot w_j^\top \mathbf{e}_t}{\|w_k\| + \eta}, \quad x \in \{h, t\}, \quad (37)$$

where  $\text{sim}$  measures the cosine similarity of the feature vectors.

Finally, knowledge distillation is applied from  $\hat{\mathbf{z}}_h$  and  $\hat{\mathbf{z}}_t$  to  $\mathbf{z}_b$ , with a balancing loss, encouraging uniform performance across all classes:

$$L_b = \kappa_h L_m(\sigma(\hat{\mathbf{z}}_h), \sigma(\mathbf{z}_b)) + \kappa_t L_m(\sigma(\hat{\mathbf{z}}_t), \sigma(\mathbf{z}_b)), \quad (38)$$

where  $\sigma$  is the softmax, and  $\kappa_h, \kappa_t$  are adaptive weights:

$$\kappa_x = \frac{(\mathcal{L}(\hat{\mathbf{z}}_x))^\alpha}{(\mathcal{L}(\hat{\mathbf{z}}_t))^\alpha + (\mathcal{L}(\hat{\mathbf{z}}_h))^\alpha}, \quad x \in \{h, t\}, \quad (39)$$

where  $\alpha$  is the scaling factor. This loss can be seen as an empirical risk minimization which distills knowledge from  $\mathcal{M}_h$  and  $\mathcal{M}_t$ . To accommodate ECG inputs, we employ ResNet18 as the common feature extraction backbone for all three models, followed by a multi-head classifier as the final classification layer.

**Reflective Label Corrector.** To improve label quality, COMIC iteratively refines the candidate label set based on model confidence. Labels with predicted probability exceeding a dynamic threshold, computed from both a global category prior and a fixed margin, are considered as positive labels, while others are either removed or retained with

lower weight. This correction step is designed to be class-aware: it scales the loss contribution using the head–tail factor so that tail-class labels receive more influence during optimization. This prevents the correction process from disproportionately favoring head classes, which naturally tend to have higher confidence predictions.

Given candidate labels  $Y_i$  for a sample, COMIC refines them using model confidence  $p_c$ . With threshold  $\tau$  and per-class average probability  $P_j$ , the updated pseudo-label  $\hat{y}_j$  is:

$$\hat{y}_j = \begin{cases} 1, & \text{if } p_c > \max\{\tau, P_j\}, y_j = 1, \\ 0, & \text{otherwise.} \end{cases} \quad (40)$$

The classification loss for each class is then:

$$L_c(p_j) = \begin{cases} L_m^+(p_j), & \hat{y}_j = 1, \\ \mathbb{1}_{(y_j=1)} L_m^+(p_j) + L_m^-(p_j), & \text{otherwise,} \end{cases} \quad (41)$$

scaled by  $\frac{B}{N_i}$ , where  $B$  is batch size and  $N_i$  is the number of corrected labels. Since corrections tend to favor head classes,  $L_c$  is additionally scaled by  $\gamma_i^{ht}$  as the inter-sample head-tail factor to upweight tail classes.

**Total Loss.** The total loss of the COMIC model combines the three core components, including MFM loss  $L_m$ , head–tail balancing loss  $L_b$ , and label correction loss  $L_c$ , as:

$$\mathcal{L}_{COMIC} = \lambda_m L_m + \lambda_b L_b + \lambda_c L_c, \quad (42)$$

where  $\lambda_m$ ,  $\lambda_b$ , and  $\lambda_c$  control the contributions of modification, balancing, and correction respectively. This formulation enables COMIC to jointly perform noise-robust disambiguation and balanced learning in the presence of long-tailed, partially labeled datasets.

## 4 Experiments

### 4.1 Dataset

We conduct our experiments on two popular publicly available ECG datasets:

**(1) PTB-XL.** The PTB-XL dataset [34] is a large-scale, publicly available clinical ECG corpus comprising 21,837 12-lead recordings from 18,885 patients. Each recording is annotated with one or more diagnostic labels, organized within a hierarchical taxonomy of five superclass categories and 24 subclass labels. In this study, we focus exclusively on the 24 subclass labels as a multi-label classification task.

**(2) Chapman (PhysioNet 2020 version).** The Chapman dataset [49] consists of 12-lead ECG recordings collected from 10,646 patients by Chapman University and Shaoxing People’s Hospital. Each recording spans 10 seconds and is sampled at 500 Hz, providing rich temporal information. For this study, we use the version released as part of the PhysioNet 2020 Challenge [1], which unifies diagnostic labels across multiple ECG datasets.

### 4.2 Candidate Label Generation

In real-world ECG diagnosis, diagnostic ambiguity often arises because an ECG recording may exhibit overlapping conditions or because different practitioners interpret the same signal differently. In a PLL setup, each ECG recording is annotated not with its exact ground-truth label set, but with a *candidate label set* that contains the true diagnosis in addition to one or more potentially incorrect labels. For example, if an ECG is annotated with atrial fibrillation (AF) and premature ventricular contraction (PVC), we may introduce an additional label such as ST-segment change, yielding

the ambiguous candidate set  $Y = \{AF, PVC, ST\}$ . This represents the diagnostic disagreement that frequently arises in clinical practice.

To construct such candidate sets in a controlled manner, we follow the PLL dataset generation protocol [32], where three parameters control introduction of label ambiguity: (1)  $p \in [0, 0.8]$  which is the proportion of samples converted into partial label form, (2)  $r \in \mathbb{N}$ , an optional fixed number that determines the number of incorrect labels added to the candidate set, and (3)  $\epsilon \in [0, 1]$ , the probability of including any given incorrect label in the candidate set.

Recall that  $\tilde{Y}_i \subseteq \mathcal{Y}$  denote the ground-truth label set for instance  $x_i$ , where  $\mathcal{Y}$  is the set of all diagnostic classes. A candidate label set  $Y_i$  is generated as:

$$Y_i = \tilde{Y}_i \cup \{y_j \in \mathcal{Y} \setminus \tilde{Y}_i \mid \mathbb{I}_i \cdot \text{Bernoulli}(\epsilon_{i,j}) = 1\}, \quad (43)$$

where  $\epsilon_{i,j}$  is the probability of including an incorrect label  $y_j$ , and  $\mathbb{I}_i \sim \text{Bernoulli}(p)$  is an indicator denoting whether  $x_i$  is annotated with partial labels. The probability  $\epsilon_{i,j}$  can be defined uniformly across classes (symmetric ambiguity, for instance randomly assigned partial labels) or conditioned on *Class-* or *Instance-Level* properties (structured ambiguity).

This formulation provides a principled mechanism for simulating diverse sources of diagnostic uncertainty, ranging from uninformative annotation errors to clinically meaningful confusions. In the following subsections, we describe the various ambiguity generation strategies.

**4.2.1 Random Ambiguity.** In this setting, incorrect labels are introduced uniformly across all classes, independent of semantic or structural relations. For each negative label  $y_j$ , the inclusion probability is fixed as  $\epsilon_{i,j} = \epsilon$ , where  $\epsilon$  is a user-defined ambiguity rate. This mechanism mimics uninformative annotation noise and serves as widely adopted benchmark in PLL literature.

**4.2.2 Class-Level Ambiguity.** To model ambiguity arising from systematic inter-class confusions in real-world scenarios, we create *Class-Level* ambiguity guided by similarities between classes of disease. Let  $T \in \mathbb{R}^{C \times C}$  denote a *Class-Level* transition matrix, where  $t_{k,z}$  represents the probability of mislabeling class  $k$  as class  $z$ . For an instance  $x_i$  with ground-truth labels  $\tilde{Y}_i$ , the probability of including label  $z$  in the candidate label set, is defined as

$$\epsilon_{i,z} = \frac{1}{|\tilde{Y}_i|} \sum_{y_k \in \tilde{Y}_i} t_{k,z}. \quad (44)$$

This formulation introduces ambiguity proportionally to inter-class similarity. We instantiate  $T$  under the following variants:

- **Treatment-Driven Ambiguity:** Classes with overlapping treatment protocols are likely to co-occur or be confused in practice. We adopt the treatment similarity matrix from the PhysioNet 2020 Challenge [1] and use it directly as  $T$ .
- **Class-Level Cardiologist-Driven Ambiguity:** To incorporate domain expertise into ambiguity generation, we construct *Class-Level* similarity matrices using features that cardiologists have identified as diagnostically significant for disease classification [21]. Each ECG sample  $x_i$  is mapped to a feature vector  $\psi(x_i)$  containing clinically significant diagnostic attributes identified in [21]. For each diagnosis class  $y_j \in \mathcal{Y}$ , we then compute a class prototype by averaging the feature vectors of all ECGs belonging to that class:

$$v_j = \frac{1}{|\mathcal{D}_j|} \sum_{x_i \in \mathcal{D}_j} \psi(x_i), \quad (45)$$

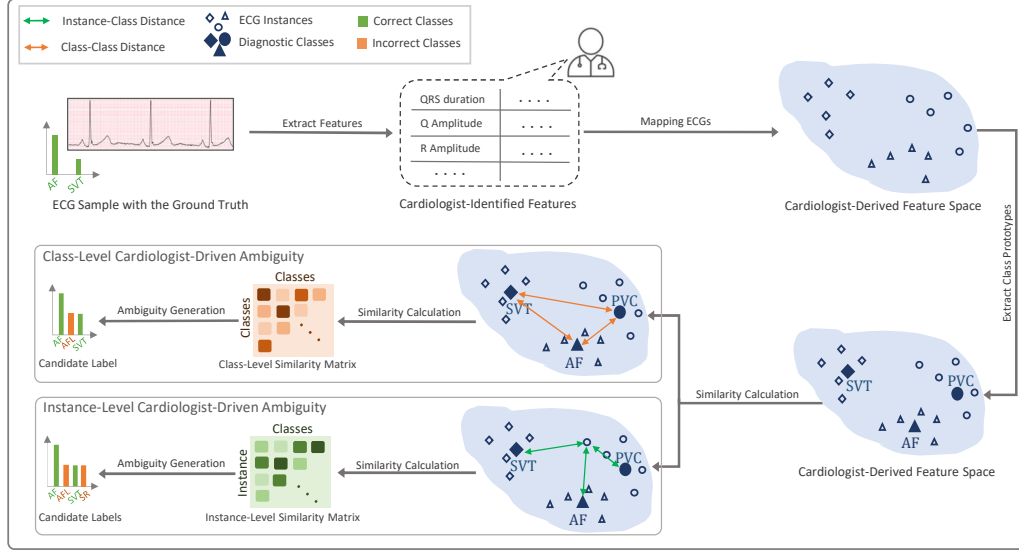


Fig. 3. Cardiologist-derived ambiguity modeling for ECG datasets. Each ECG recording is represented by clinically significant diagnostic features such as QRS duration, Q amplitude, and R amplitude. These features form a cardiologist-derived feature space, where class prototypes represent each diagnostic class. Pairwise cosine similarities between class prototypes create a *Class-Level* similarity matrix (orange), reflecting global confusion between diagnostic classes. Similarly, the cosine similarities between each individual ECG and class prototypes produce an *Instance-Level* similarity matrix (green), which captures patient-specific diagnostic ambiguity.

where  $\mathcal{D}_j$  is the set of all samples with ground-truth label  $y_j$ . Pairwise similarities between class prototypes are computed using cosine similarity, resulting in the transition matrix  $T$  that captures clinically meaningful inter-class relationships (illustrated in Fig. 3). Since raw cosine similarities vary in scale, we apply min–max normalization to ensure comparability across classes:

$$t_{j,k} = \frac{\hat{t}_{j,k} - \min(T)}{\max(T) - \min(T)}. \quad (46)$$

This normalization maps similarity values into a standardized range of  $[0, 1]$  while preserving relative differences between classes. The resulting matrix  $T$  highlights cardiologist-derived diagnostic ambiguities, which is subsequently used to guide candidate label generation.

- **Taxonomy-Driven Ambiguity:** To incorporate domain taxonomies into ambiguity generation, we restrict candidate label ambiguity to sibling classes within the diagnostic hierarchy. Intuitively, ECG classes that share the same superclass (e.g., IRBBB and CRBBB) are more likely to be misdiagnosed in practice.

Formally, for each class  $y_j \in \mathcal{Y}$ , the transition probabilities in  $T$  are defined as:

$$t_{j,k} = \begin{cases} \epsilon, & \text{if } \text{Sup}(y_j) = \text{Sup}(y_k), \\ 0, & \text{otherwise,} \end{cases} \quad (47)$$

where  $\text{Sup}(y_j)$  denotes the superclass of  $y_j$  in the diagnostic taxonomy, and  $\epsilon$  is a fixed ambiguity rate (set to 0.5 in our experiments). This formulation ensures that ambiguity reflects clinically plausible confusion patterns while avoiding unrealistic cross-superclass errors.

**4.2.3 Instance-Level Ambiguity.** To account for ambiguity at the individual patient level, we further extend label ambiguity modeling to *Instance-Level* distributions. Let  $T \in \mathbb{R}^{n \times C}$  denote an *Instance-Level* transition matrix, where  $t_{i,k}$  is the probability of including class  $k$  for instance  $x_i$ . We consider two biologically motivated variants of this type of ambiguity:

- **Instance-Level Cardiologist-Driven Ambiguity:** To capture ambiguity at the level of individual ECG recordings, we extend the *Class-Level* Cardiologist-Derived similarity to an *Instance-Level* formulation. For each ECG  $x_i$ , we extract its feature vector  $\psi(x_i)$  based on cardiologist-identified diagnostic attributes [21]. This instance representation is then compared with each class prototype  $v_j$  (Fig. 3) using cosine similarity, producing a similarity distribution  $t_{i,\cdot}$  over all classes. Finally, the scores are standardized via the min–max normalization procedure.
- **Model-Driven Ambiguity:** Inspired by pseudo-labeling techniques in PLL [42, 43], we leverage the confidence scores of a classifier  $f(\cdot; \theta)$  trained on clean ground-truth labels to simulate ambiguity. For a given instance  $x_i$  and an incorrect class  $y_k$ , the *Instance-Level* transition matrix is defined as

$$t_{i,k} = \frac{f_k(x_i; \theta)}{\max_{y_j \in \mathcal{Y} \setminus \tilde{Y}_i} f_j(x_i; \theta)} \quad \text{for } y_k \in \mathcal{Y} \setminus \tilde{Y}_i, \quad (48)$$

where  $f_j(x_i; \theta)$  denotes the predicted probability for class  $y_j$ . This formulation scales the confidence of each incorrect class relative to the most confident incorrect prediction, yielding a normalized distribution over potential false positives.

### 4.3 Implementation and Evaluation Details

All baseline models are implemented within a unified framework to ensure fair and consistent comparison. We adopt a 1D ResNet18 as the shared backbone architecture for all PLL methods, composed of four stages with two bottleneck blocks each. Each bottleneck block contains three convolutional layers: a  $1 \times 1$  convolution for channel reduction, a  $3 \times 3$  convolution (stride 1 for the first stage and 2 for the remaining stages) with padding 1, and a final  $1 \times 1$  convolution to restore channels. Batch normalization and ReLU activation follow each convolutional layer, except the last, where ReLU is applied after residual addition. The final feature map is reduced via adaptive average pooling to a single value per channel and passed through a fully connected layer to produce the outputs. Training is conducted using a batch size of 32, a learning rate of 0.001, and the RMSprop [ ] optimizer with default momentum settings over 20 epochs. Each method follows its original network and parameter configuration as closely as possible. All experiments are conducted in PyTorch on an NVIDIA RTX 2080 GPU.

To evaluate performance under partial supervision, we adopt micro-F1 and AUROC as widely used metrics in ECG classification [ ]. The results are reported on a clean held-out test set, while training is performed on versions of the training set augmented with varying levels of label ambiguity introduced by the six candidate label generation strategies described in Section 4.2. We repeat each experiment across three random seeds, and report the mean and standard deviation of both metrics to assess robustness. The full code will be made publicly available upon publication.

For the PTB-XL dataset, we apply all candidate label generation strategies described in Section 4.2. For the *Class-Level Treatment-Driven* strategy, we adopt label definitions from the PhysioNet 2020 Challenge [1] to leverage clinically curated inter-class dependency weights, enabling a more realistic modeling of diagnostic ambiguity. For the *Cardiologist-Driven* strategies, we use the diagnostic features provided for PTB-XL in [31]. In contrast, for the Chapman dataset (PhysioNet 2020 version), the available label schema supports only a subset of ambiguity strategies. Specifically, we

Table 3. Comparison of baseline models under different partial label generation methods for PTB-XL dataset. Bold numbers denote the best performance, while underline indicates the second best.

Baseline Models	Random -	Instance-Level		Class-Level		
		Cardiologist-Driven	Model-Driven	Cardiologist-Driven	Taxonomy-Driven	Treatment-Driven
<b>No PLL</b>	0.432±0.024	0.383±0.042	0.289±0.012	0.39±0.044	0.611±0.008	0.520±0.041
<b>DNPL [27]</b>	<u>0.621±0.001</u>	<u>0.609±0.004</u>	<u>0.617±0.003</u>	<u>0.620±0.004</u>	0.615±0.006	0.677±0.010
<b>PRODEN [19]</b>	<b>0.638±0.008</b>	<b>0.637±0.008</b>	<b>0.624±0.009</b>	<b>0.637±0.011</b>	0.638±0.002	<u>0.747±0.001</u>
<b>CAVL [45]</b>	0.595±0.003	0.586±0.006	0.594±0.006	0.583±0.011	0.612±0.003	0.685±0.004
<b>LW [39]</b>	0.599±0.008	0.593±0.006	0.608±0.004	0.599±0.003	0.590±0.008	0.736±0.001
<b>CR [40]</b>	0.534±0.013	0.506±0.016	0.526±0.020	0.524±0.013	0.530±0.008	0.730±0.003
<b>PICO [36]</b>	0.524±0.030	0.543±0.005	0.527±0.022	0.552±0.006	0.554±0.003	0.690±0.004
<b>SST [4]</b>	0.474±0.047	0.409±0.039	0.401±0.025	0.502±0.043	0.632±0.009	0.694±0.024
<b>HST [3]</b>	0.472±0.058	0.498±0.048	0.293±0.025	0.545±0.011	<u>0.644±0.010</u>	0.717±0.023
<b>COMIC [48]</b>	0.532±0.020	0.542±0.016	0.320±0.017	0.525±0.026	<b>0.687±0.005</b>	<b>0.754±0.003</b>

Table 4. Comparison of PLL baseline models under different candidate label generation methods for Chapman dataset. Bold numbers denote the best performance, while underline indicates the second best.

Baseline Models	Random -	Instance-Level	Class-Level
		Model-Driven	Treatment-Driven
<b>No PLL</b>	0.543±0.045	0.395±0.024	0.556±0.046
<b>DNPL [27]</b>	<u>0.726±0.009</u>	<u>0.728±0.012</u>	0.730±0.006
<b>PRODEN [19]</b>	0.671±0.010	0.689±0.008	0.689±0.007
<b>CAVL [45]</b>	0.656±0.019	0.712±0.014	0.684±0.010
<b>LW [39]</b>	0.725±0.012	0.719±0.011	0.708±0.001
<b>CR [40]</b>	0.691±0.014	0.682±0.013	0.701±0.017
<b>PICO [36]</b>	<b>0.740±0.006</b>	<b>0.734±0.006</b>	0.737±0.002
<b>SST [4]</b>	0.614±0.066	0.51±0.081	<u>0.761±0.010</u>
<b>HST [3]</b>	0.718±0.053	0.347±0.027	<b>0.773±0.005</b>
<b>COMIC [48]</b>	0.643±0.036	0.371±0.007	0.751±0.033

generate candidate labels using the *Treatment-Driven*, *Random*, and *Model-Driven* ambiguity strategies, while other variants that rely on explicit hierarchical taxonomies or cardiologist crafted features are not applicable to this dataset.

#### 4.4 Performance Comparison

Tables 3 and 4 report the classification performance (F1 score) of nine state-of-the-art PLL models, along with a *No PLL* baseline, under the three major candidate label generation strategies: *Random*, *Instance-Level* (*Cardiologist-Driven* and *Model-Driven*), and *Class-Level* (*Cardiologist-Driven*, *Taxonomy-Driven*, and *Treatment-Driven*). Experiments are conducted on the PTB-XL and Chapman ECG datasets with 50% of the training samples partially labeled ( $p = 0.5$ ). This comprehensive evaluation provides insight into the robustness of each method under different ambiguity structures. On PTB-XL (Table 3), most PLL methods outperform the *No PLL* baseline, confirming the benefit of equipping models with PLL components under partial supervision. Among them, PRODEN delivers the most consistent and

competitive performance across nearly all ambiguity scenarios. Its robustness highlights the effectiveness of iterative label distribution refinement for managing ambiguity in multi-label ECG diagnosis. LW and CR exhibit relatively strong performance, especially in scenarios involving *Class-Level* ambiguities, suggesting that their reliance on negative supervision and consistency regularization effectively enhances label disambiguation. By contrast, SST and HST display notable degradation under *Instance-Level* ambiguity, underscoring their limited adaptability beyond image-based assumptions. This could be attributed to their dependence on semantic embeddings for class relation extraction, which constrains their effectiveness when the embeddings are less informative. COMIC presents an interesting contrast: although weaker under random and *Instance-Level* ambiguities, it achieves top performance under Treatment-Driven ambiguity. This demonstrates the benefit of its correction–modification mechanism when ambiguities simulate clinical relationships.

On the Chapman dataset (Table 4), we observe a different trend. PICO consistently ranks among the best-performing methods, while simple approaches such as DNPL and LW also remain competitive. Notably, all PLL methods outperform the *No PLL* baseline, again validating the usefulness of considering label ambiguities. The strongest gains are observed under *Treatment-Driven* ambiguity, where several methods (including COMIC, HST, and SST) outperform their results under *Random* or *Instance-Level* ambiguity. This suggests that when candidate labels reflect clinically grounded confusion patterns, PLL models can more effectively leverage structure to disambiguate. However, the instability of HST and SST persists similar to the results on the PTB-XL dataset.

Overall, we make the following observations. First, while certain methods perform better in specific ambiguity scenarios, models that maintain stable performance across multiple conditions (such as DNPL or PRODEN) are more desirable for real-world ECG applications with varying types of ambiguity. Second, the differing trends observed across PTB-XL and Chapman suggest that dataset characteristics (e.g., class granularity, label distribution, or inherent noise) can significantly impact the effectiveness of PLL methods. This highlights the importance of benchmarking PLL frameworks under diverse datasets and ambiguity structures to fully understand their robustness. Finally, the results of the *No PLL* baseline highlights the negative impact of not considering label ambiguities. This emphasizes the necessity of integrating PLL frameworks, or similar ambiguity-aware learning strategies, into practical diagnostic systems.

#### 4.5 Sensitivity Analysis to Partial Label Proportion

To further investigate the robustness of baseline models to varying levels of label ambiguity, we conduct a series of controlled experiments by varying the proportion of ambiguous instances ( $p \in [0, 0.8]$ ). The corresponding results for the PTB-XL and Chapman datasets are presented in Figures 4 and 5, respectively, while Figure 6 provides an additional analysis with *Random* ambiguity by jointly varying the false-label inclusion probability ( $\epsilon$ ) and the ambiguity proportion ( $p$ ). Across all configurations, we observe that the performance of PLL models gradually degrades as the proportion of ambiguous samples increases, with (*No PLL*) showing a severe performance drop, highlighting the vulnerability of conventional supervised training on ambiguous ECG annotations.

As shown in Figure 4, the performance of most PLL methods consistently degrades as  $p$  increases. Among the candidate label generation strategies, the *Taxonomy-Driven* ambiguity (Fig. 4d) is the least challenging, suggesting that this strategy induces weaker forms of ambiguity. In contrast, ambiguity introduced through *Cardiologist-Driven* on *Class-Level* and *Instance-Level* strategies (Figs. 4b–c) leads to considerable performance declines, which shows the difficulty of resolving ambiguities based on cardiologist interpretation. Notably, methods such as DNPL and PRODEN consistently outperform others and demonstrate more stable performance. A similar pattern is observed on the Chapman dataset. Under *Treatment-Driven* ambiguity, most PLL methods maintain strong performance even at higher levels of  $p$

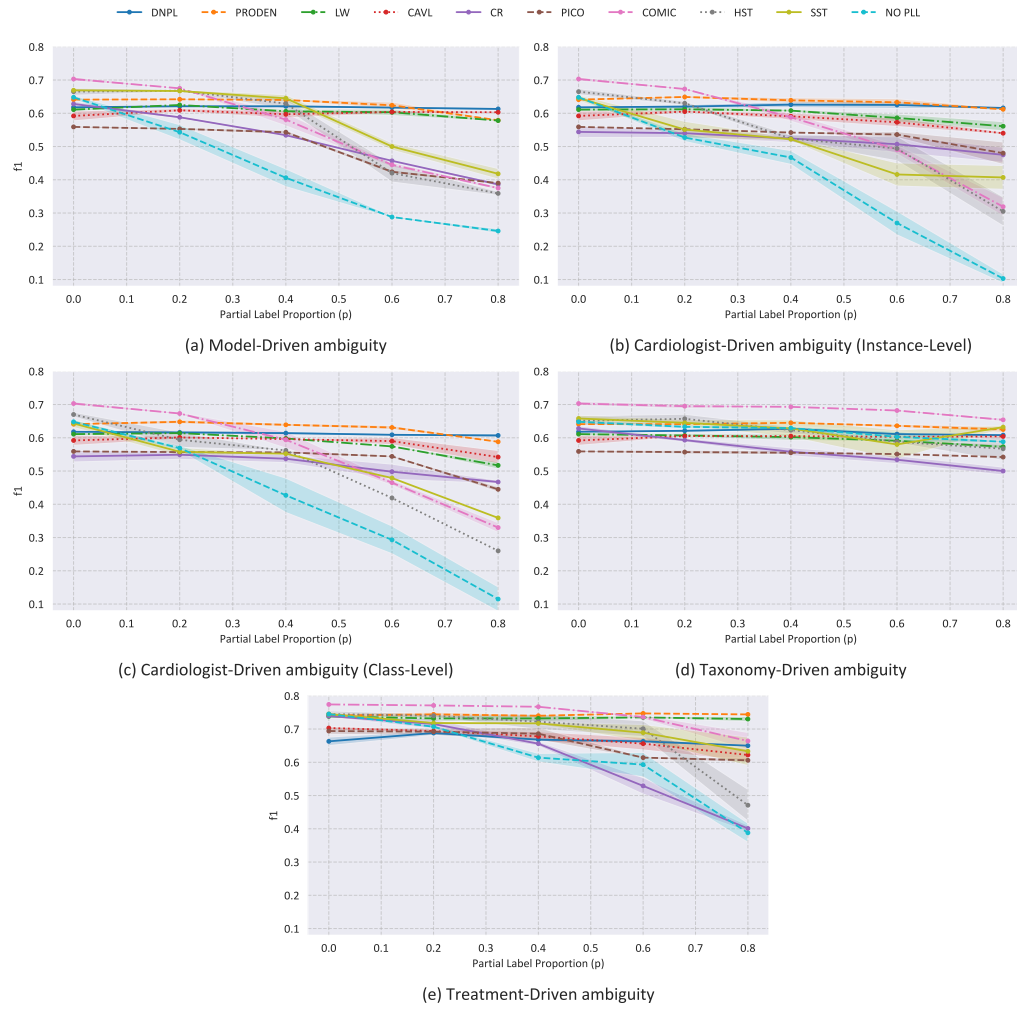


Fig. 4. Baseline performance over different proportions of ambiguous samples ( $p$ ) for PTB-XL dataset.

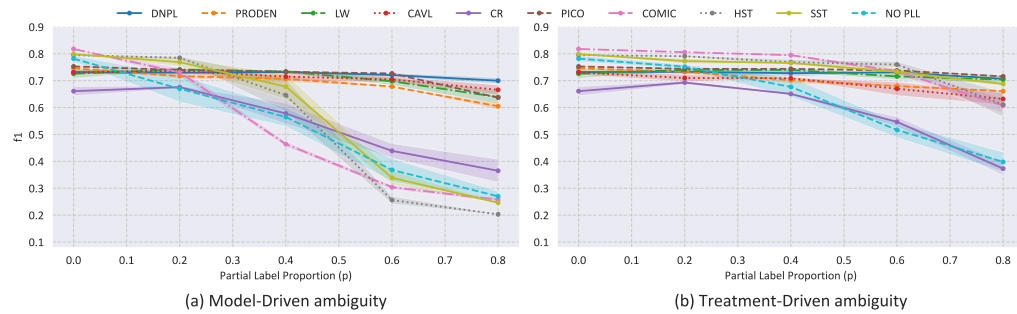


Fig. 5. Baseline performance over different proportions of ambiguous samples ( $p$ ) for Chapman dataset.

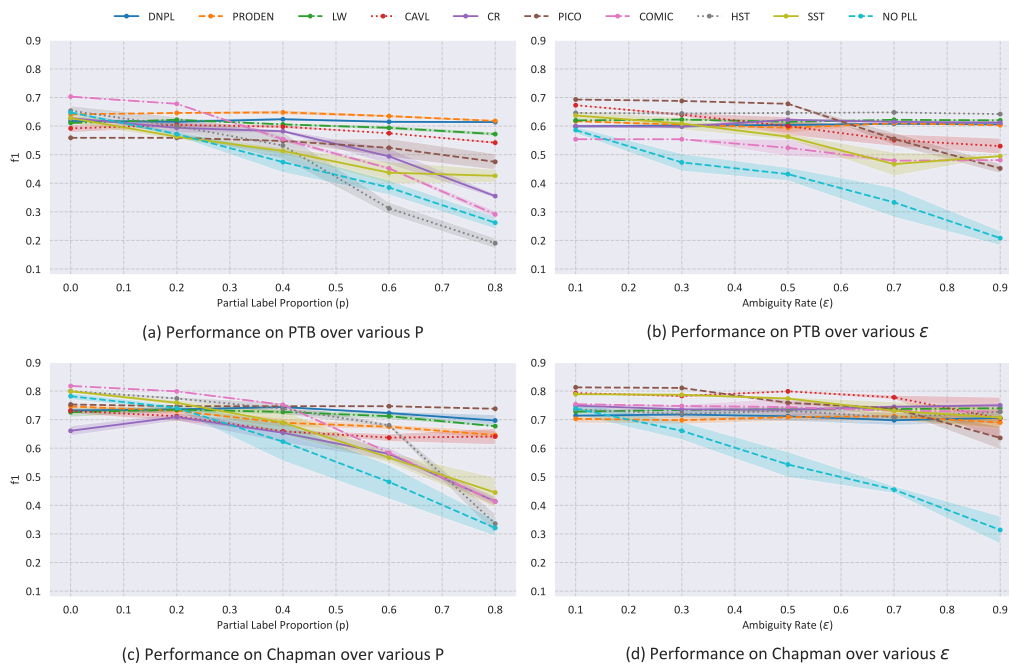


Fig. 6. Baseline performance on random ambiguity over different proportions of ambiguous samples ( $p$ ) and rates of ambiguity.

(up to  $p = 0.8$ ). For *Model-Driven* ambiguity, approaches like SST and CR show more degradation. This suggests that PLL models relying heavily on structural or semantic priors may struggle when ambiguity arises at the *Instance-Level* rather than from systematic class overlaps.

We further analyze the impact of  $p$  and  $\epsilon$  in Fig. 6. Specifically, we fix  $\epsilon = 0.5$  to examine the effect of increasing the proportion of ambiguous samples (Figs. 6a and 6c), and fix  $p = 0.5$  to assess the effect of varying the number of false labels within each instance during training (Figs. 6b and 6d). The results show that increasing both parameters leads to performance degradation across all methods, although PLL models experience a noticeably slower decline when  $\epsilon$  increases for both datasets. DNPL and PRODEN again demonstrate more robustness to varying levels of ambiguity. Interestingly, most PLL models are more sensitive to the amount of ambiguous samples ( $p$ ) than to the degree of noise within each sample ( $\epsilon$ ). These findings suggest that while existing PLL approaches can tolerate moderate diagnostic ambiguity, their stability strongly depends on the structure and scale of ambiguity. In contrast, models trained without ambiguity-aware mechanisms exhibit sharp performance drops as ambiguity increases.

#### 4.6 Quantitative Analysis of Ambiguity in Candidate Label Generation Strategies

We quantitatively examine the degree of ambiguity introduced by different candidate label generation strategies under varying proportions of ambiguous instances ( $p$ ), as illustrated in Fig. 7. To capture this effect, we report the *flip probability*, defined as the average probability of including a false label, computed as the ratio of false positive labels to the total number of negative labels within each instance. As shown in Fig. 7a, the *Random*, *Model-Driven*, and *Instance-Level Cardiologist-Driven* strategies produce higher ambiguity levels compared to the *Taxonomy-Driven* approach, which

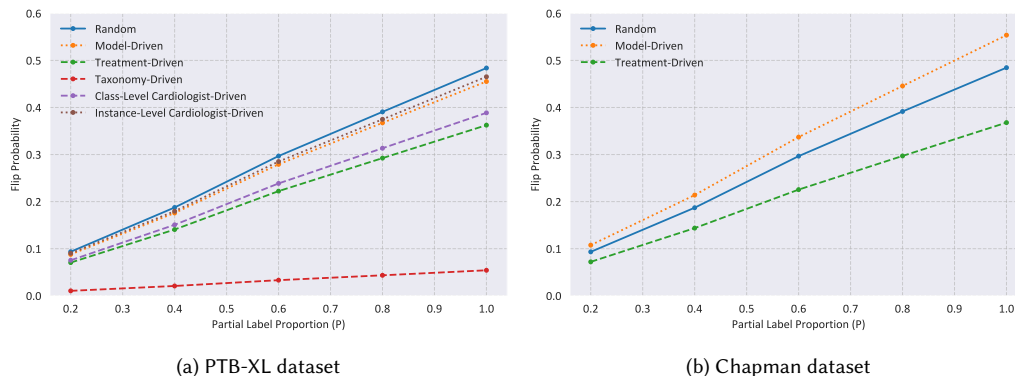


Fig. 7. Flip probability across candidate label generation strategies for different proportions of ambiguous samples ( $p$ ) on the PTB-XL and Chapman datasets.

demonstrates notably lower flip probabilities. This outcome aligns with expectations, since taxonomy-based candidate labels are constrained by class hierarchies and therefore remain closer to the true annotations.

While the *Treatment-Driven* and *Class-Level Cardiologist-Driven* strategies introduce a similar degree of ambiguity, models tend to struggle more with the latter (As observed in Fig. 4). This suggests that beyond the amount of ambiguity, its underlying structure substantially influence how models perform. Finally, the results on the Chapman dataset (Fig. 7b) follow the same pattern observed for PTB-XL, showing consistency between the amount of ambiguity (flip probability) and decrease in models performance (Fig. 5). Overall, these findings highlight the importance of considering both the type and the amount of ambiguity when generating candidate labels for a comprehensive evaluation of PLL models.

#### 4.7 Class-Specific Analysis of PLL Baselines

To further understand how ambiguity affects different diagnostic categories, we analyze the class-specific performance of PLL methods on the PTB-XL and Chapman datasets, as illustrated in Figs. 8 and 9. In this analysis, we sort classes by their instance count in the dataset, such that classes with higher count appear toward the top of the heatmaps. The results reveal that the impact of ambiguity is highly class-dependent. Overall, major classes show lower sensitivity to ambiguity, while minor classes experience more pronounced degradation across both datasets. In the PTB-XL dataset, classes such as *IMI* and *STTC* maintain consistently strong performance across ambiguity types, suggesting that their distinctive characteristics make them less prone to ambiguity. In contrast, classes such as *WPW* and *IVCD* show significant performance degradation, despite having relatively higher sample counts than some more robust classes (e.g., *IMI*, *STTC*). This suggests that their diagnostic complexity makes them sensitive to ambiguity. Among the PLL baselines, *COMIC* demonstrates the most consistent performance across the majority of classes, likely due to their ability to handle class-imbalance.

A similar trend is observed for the Chapman dataset, where major classes remain among the most robust, while minor classes are more prone to ambiguity. Once again, *COMIC* maintains more balanced performance across both major and minor classes compared to other baselines. Interestingly, methods originally designed for multi-label settings, such as *HST* and *SST*, display relatively stable behavior across classes under *Model-Driven* ambiguity but decline under

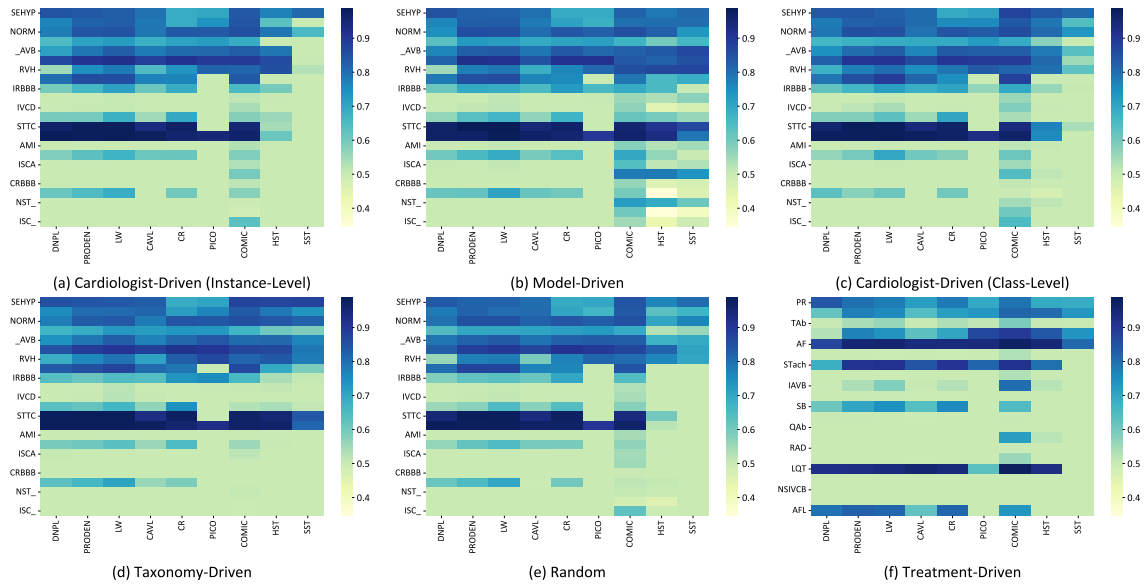


Fig. 8. Study of class-specific performance of PLL methods on PTB-XL dataset.

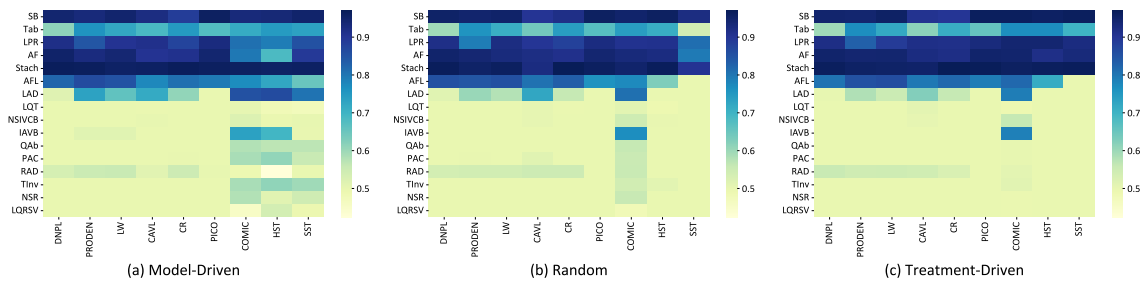


Fig. 9. Study of class-specific performance of PLL methods on Chapman dataset.

other ambiguity types. Collectively, these findings highlight that while models such as *DNPL* and *PRODEN* achieve high overall performance in aggregated metrics (micro F1), their class-level robustness can vary considerably.

**4.8 Limitations and Future Work**

While this work provides the first systematic study of adapting PLL methods to ECG diagnosis, several limitations remain. First, although our candidate label generation strategies are motivated by clinical reasoning, future work should explore using candidate labels arising from real-world diagnostic ambiguities. Second, for methods that rely on data augmentation (e.g., contrastive learning or consistency regularization), we restrict our experiments to additive Gaussian noise. Exploring a broader set of ECG-specific augmentations may enhance the performance of these approaches. Additionally, future work could explore a wider variety of encoder backbones to better understand the impact of specific network architectures on performance. Another limitation comes from the standard PLL assumption that the ground-truth label is always included in the candidate set. In real clinical scenarios, annotation errors may exclude the

correct label entirely, which is not simulated in the current study. This could be explored in future studies where the correct label could be missing from candidate label sets. Our findings highlight several directions for ambiguity-aware learning in ECG analysis. For instance, we observed that sensitivity to hyperparameters limits the generalization of PLL methods in different scenarios. Future work should develop models that are less dependent on hyperparameter choice to ensure generalizability to various ambiguity scenarios in clinical settings. Additionally, many PLL methods show performance degradation on minor classes which could be addressed in future studies.

## 5 Conclusion

In this work, we present a comprehensive study of PLL methods for ECG diagnosis under diagnostic ambiguity. We adapt nine PLL algorithms, originally developed for computer vision tasks, to ECG diagnosis and evaluate them across different types of ambiguity including random, class-dependent (e.g., treatment similarity, disease taxonomy, and cardiologist driven), and instance dependent (model and cardiologist driven). Our analysis shows that different PLL methods perform differently in dealing with different forms of ambiguity. Specifically, we find that PLL methods outperform classical solutions that do not explicitly consider label ambiguities, with DNPL and PRODEN generally outperforming other PLL approaches. Our class-specific analysis highlights that the type of label ambiguity largely affects the minority classes, which shows the importance of considering class imbalance in designing and evaluating PLL methods for ECG diagnosis. Overall, our study establishes a foundation for ECG diagnosis with label ambiguities which could arise in many real-world scenarios. We identify key limitations of existing PLL approaches and outline several promising directions. We hope our work encourages the development of next-generation PLL frameworks tailored to the challenges of clinical annotation and supports the creation of more robust ECG diagnostic systems.

## Acknowledgments

We would like to thank the Natural Sciences and Engineering Research Council of Canada (NSERC) and Ingenuity Labs Research Institute for partially funding and supporting this work.

## References

- [1] E. A. P. Alday, A. Gu, A. J. Shah, C. Robichaux, A.-K. I. Wong, C. Liu, F. Liu, A. B. Rad, A. Elola, and S. Seyedi. 2020. Classification of 12-lead eegs: the physionet/computing in cardiology challenge 2020. *Physiological Measurement* 41, 12 (2020).
- [2] M. Ashhad, S. Rahmani, M. Fayiz, A. Etamad, and J. Hashemi. 2024. Uncertainty-Aware Multi-view Arrhythmia Classification from ECG. In *International Joint Conference on Neural Networks*. 1–6.
- [3] T. Chen, T. Pu, L. Liu, Y. Shi, Z. Yang, and L. Lin. 2024. Heterogeneous semantic transfer for multi-label recognition with partial labels. *International Journal of Computer Vision* 132, 12 (2024), 6091–6106.
- [4] T. Chen, T. Pu, H. Wu, Y. Xie, and L. Lin. 2022. Structured semantic transfer for multi-label recognition with partial labels. In *Proceedings of the AAAI Conference on Artificial Intelligence*, Vol. 36. 339–346.
- [5] T. Chen, M. Xu, X. Hui, H. Wu, and L. Lin. 2019. Learning semantic-specific graph representation for multi-label image recognition. In *Proceedings of the IEEE/CVF International Conference on Computer Vision*. 522–531.
- [6] M. Cuturi. 2013. Sinkhorn distances: Lightspeed computation of optimal transport. *Advances in Neural Information Processing Systems* 26 (2013).
- [7] T. Durand, N. Mehrasa, and G. Mori. 2019. Learning a deep convnet for multi-label classification with partial labels. In *Proceedings of the IEEE/CVF Conference on Computer Vision and Pattern Recognition*. 647–657.
- [8] J. Feng, Q. Guo, S. Luo, L. Chen, and Q. Ma. 2024. Blood Cell Attribute Classification Algorithm Based on Partial Label Learning. *Electronics* 13, 9 (2024).
- [9] C. S. Grubb, L. Melki, D. Y. Wang, J. Peacock, J. Dizon, V. Iyer, C. Sorbera, A. Biviano, D. A. Rubin, and J. P. Morrow. 2020. Noninvasive localization of cardiac arrhythmias using electromechanical wave imaging. *Science Translational Medicine* 12, 536 (2020).
- [10] A. Y. Hannun, P. Rajpurkar, M. Haghpanahi, G. H. Tison, C. Bourn, M. P. Turakhia, and A. Y. Ng. 2019. Cardiologist-level arrhythmia detection and classification in ambulatory electrocardiograms using a deep neural network. *Nature Medicine* 25, 1 (2019), 65–69.

- [11] L. S. Johnson, P. Zadrozniak, G. Jasina, A. Grotek-Cuprjak, J. G. Andrade, E. Svennberg, S. Z. Diederichsen, W. F. McIntyre, S. Stavrakis, and J. Benezet-Mazuecos. 2025. Artificial intelligence for direct-to-physician reporting of ambulatory electrocardiography. *Nature Medicine* (2025), 1–7.
- [12] Y. Kim, J. M. Kim, Z. Akata, and J. Lee. 2022. Large loss matters in weakly supervised multi-label classification. In *Proceedings of the IEEE/CVF Conference on Computer Vision and Pattern Recognition*. 14156–14165.
- [13] K. Li, L. Yu, and P.-A. Heng. 2022. Domain-incremental cardiac image segmentation with style-oriented replay and domain-sensitive feature whitening. *IEEE Transactions on Medical Imaging* 42, 3 (2022), 570–581.
- [14] W. Li, L. Fan, S. Shao, and A. Song. 2024. Generalized contrastive partial label learning for cross-subject EEG-based emotion recognition. *IEEE Transactions on Instrumentation and Measurement* (2024).
- [15] Y. Li, D. Tarlow, M. Brockschmidt, and R. Zemel. 2016. Gated graph sequence neural networks. *International Conference on Learning Representations* (2016).
- [16] T.-Y. Lin, P. Goyal, R. Girshick, K. He, and P. Dollár. 2017. Focal loss for dense object detection. In *Proceedings of the IEEE International Conference on Computer Vision*. 2980–2988.
- [17] W. Liu, S. Pan, Z. Li, S. Chang, Q. Huang, and N. Jiang. 2024. Bootstrap each lead’s latent: a novel method for self-supervised learning of multilead electrocardiograms. *Computer Methods and Programs in Biomedicine* 257 (2024).
- [18] Z.-Y. Liu, C.-H. Lin, Y.-C. Hsu, J.-S. Chen, P.-C. Chang, M.-S. Wen, and C.-F. Kuo. 2025. Universal representations in cardiovascular ECG assessment: A self-supervised learning approach. *International Journal of Medical Informatics* 195 (2025).
- [19] J. Lv, M. Xu, L. Feng, G. Niu, X. Geng, and M. Sugiyama. 2020. Progressive identification of true labels for partial-label learning. In *International Conference on Machine Learning*. PMLR, 6500–6510.
- [20] S. Matsuo, D. Suehiro, S. Uchida, H. Ito, K. Terada, A. Yoshizawa, and R. Bise. 2024. Learning from Partial Label Proportions for Whole Slide Image Segmentation. In *International Conference on Medical Image Computing and Computer-Assisted Intervention*. Springer, 372–382.
- [21] T. Mehari, A. Sundar, A. Bosnjakovic, P. Harris, S. E. Williams, A. Loewe, O. Doessel, C. Nagel, N. Strodthoff, and P. J. Aston. 2024. Ecg feature importance rankings: Cardiologists vs. algorithms. *IEEE Journal of Biomedical and Health Informatics* 28, 4 (2024), 2014–2024.
- [22] Sana Rahmani, Reetam Chatterjee, Ali Etemad, and Javad Hashemi. 2025. Dynamic Prototype Rehearsal for Continual ECG Arrhythmia Detection. In *IEEE International Conference on Acoustics, Speech and Signal Processing*. IEEE, 1–5.
- [23] E. Ribeiro, Q. B. Soares, F. M. Dias, J. E. Krieger, and M. A. Gutierrez. 2023. Can deep learning models differentiate atrial fibrillation from atrial flutter? *medRxiv* (2023).
- [24] P. B. Rigueira, G. H. G. Evangelista, L. G. Porfirio, C. S. Grossi, A. Buzelin, G. L. Pappa, G. M. M. Paixao, A. Ribeiro, and W. Meira Jr. 2024. Optimizing ECG Audits: Clustering-Based Identification of Ambiguous Exams. In *Encontro Nacional de Inteligência Artificial e Computacional*. SBC, 61–72.
- [25] R. R. Selvaraju, M. Cogswell, A. Das, R. Vedantam, D. Parikh, and D. Batra. 2020. Grad-CAM: visual explanations from deep networks via gradient-based localization. *International Journal of Computer Vision* 128 (2020), 336–359.
- [26] M. Senoussi, T. Artieres, and P. Villoutreix. 2024. Partial label learning for automated classification of single-cell transcriptomic profiles. *PLOS Computational Biology* 20, 4 (2024).
- [27] J. Seo and J. S. Huh. 2021. On the power of deep but naive partial label learning. In *IEEE International Conference on Acoustics, Speech and Signal Processing*. 3820–3824.
- [28] J. Shi, W. Liu, H. Zhang, S. Chang, H. Wang, J. He, and Q. Huang. 2024. CPSS: Fusing consistency regularization and pseudo-labeling techniques for semi-supervised deep cardiovascular disease detection using all unlabeled electrocardiograms. *Computer Methods and Programs in Biomedicine* 254 (2024).
- [29] S. Soltanieh, A. Etemad, and J. Hashemi. 2022. Analysis of augmentations for contrastive ecg representation learning. In *International Joint Conference on Neural Networks*. 1–10.
- [30] S. Soltanieh, J. Hashemi, and A. Etemad. 2023. In-distribution and out-of-distribution self-supervised ecg representation learning for arrhythmia detection. *IEEE Journal of Biomedical and Health Informatics* (2023).
- [31] N. Strodthoff, T. Mehari, C. Nagel, P. J. Aston, A. Sundar, C. Graff, J. K. Kanters, W. Haverkamp, O. Dössel, and A. Loewe. 2023. PTB-XL+, a comprehensive electrocardiographic feature dataset. *Scientific Data* 10, 1 (2023).
- [32] Y. Tian, X. Yu, and S. Fu. 2023. Partial label learning: Taxonomy, analysis and outlook. *Neural Networks* 161 (2023), 708–734.
- [33] B. Vandenberg, T. Robyns, G. Goovaerts, M. Claeys, F. Helsen, S. Van Soest, C. Garweg, J. Ector, S. Van Huffel, and R. Willems. 2018. Inter- and intra-observer variability of visual fragmented QRS scoring in ischemic and non-ischemic cardiomyopathy. *Journal of Electrocardiology* 51, 3 (2018), 549–554.
- [34] P. Wagner, N. Strodthoff, R.-D. Bousselet, D. Kreiseler, F. I. Lunze, W. Samek, and T. Schaeffter. 2020. PTB-XL, a large publicly available electrocardiography dataset. *Scientific Data* 7, 1 (2020).
- [35] H. Wang, M. Xia, Y. Li, Y. Mao, L. Feng, G. Chen, and J. Zhao. 2022. Solar: Sinkhorn label refinery for imbalanced partial-label learning. *Advances in Neural Information Processing Systems* 35 (2022), 8104–8117.
- [36] H. Wang, R. Xiaoy, Y. Li, L. Feng, G. Niu, G. Chen, and J. Zhao. 2022. Pico: Contrastive label disambiguation for partial label learning. In *International Conference on Learning Representations*.
- [37] R. Wang, Q. Yao, X. Fan, and Y. Li. 2019. Multi-class arrhythmia detection based on neural network with multi-stage features fusion. In *IEEE International Conference on Systems, Man and Cybernetics*. 4082–4087.

- [38] W. Wang, L. Feng, Y. Jiang, G. Niu, M.-L. Zhang, and M. Sugiyama. 2024. Binary classification with confidence difference. *Advances in Neural Information Processing Systems* 36 (2024).
- [39] H. Wen, J. Cui, H. Hang, J. Liu, Y. Wang, and Z. Lin. 2021. Leveraged weighted loss for partial label learning. In *International Conference on Machine Learning*. PMLR, 11091–11100.
- [40] D.-D. Wu, D.-B. Wang, and M.-L. Zhang. 2022. Revisiting consistency regularization for deep partial label learning. In *International Conference on Machine Learning*. PMLR, 24212–24225.
- [41] J.-H. Wu, X. Wu, Q.-G. Chen, Y. Hu, and M.-L. Zhang. 2020. Feature-induced manifold disambiguation for multi-view partial multi-label learning. In *ACM SIGKDD International Conference on Knowledge Discovery and Data Mining*. 557–565.
- [42] N. Xu, C. Qiao, X. Geng, and M.-L. Zhang. 2021. Instance-dependent partial label learning. *Advances in Neural Information Processing Systems* 34 (2021), 27119–27130.
- [43] N. Xu, C. Qiao, Y. Zhao, X. Geng, and M.-L. Zhang. 2024. Variational label enhancement for instance-dependent partial label learning. *IEEE Transactions on Pattern Analysis and Machine Intelligence* (2024).
- [44] Q. Yao, R. Wang, X. Fan, J. Liu, and Y. Li. 2020. Multi-class arrhythmia detection from 12-lead varied-length ECG using attention-based time-incremental convolutional neural network. *Information Fusion* 53 (2020), 174–182.
- [45] F. Zhang, L. Feng, B. Han, T. Liu, G. Niu, T. Qin, and M. Sugiyama. 2021. Exploiting class activation value for partial-label learning. In *International Conference on Learning Representations*.
- [46] G. Zhang and A. Etemad. 2025. Partial label learning for emotion recognition from EEG. *IEEE Transactions on Affective Computing* (2025).
- [47] S. Zhang, C. Lian, B. Xu, Y. Su, and A. Alhudhaif. 2024. 12-Lead ECG signal classification for detecting ECG arrhythmia via an information bottleneck-based multi-scale network. *Information Sciences* 662 (2024).
- [48] W. Zhang, C. Liu, L. Zeng, B. Ooi, S. Tang, and Y. Zhuang. 2023. Learning in imperfect environment: Multi-label classification with long-tailed distribution and partial labels. In *Proceedings of the IEEE/CVF International Conference on Computer Vision*. 1423–1432.
- [49] J. Zheng, J. Zhang, S. Danioko, H. Yao, H. Guo, and C. Rakovski. 2020. A 12-lead electrocardiogram database for arrhythmia research covering more than 10,000 patients. *Scientific Data* 7, 1 (2020), 48.